Status of Modifications to the AGR-3/4 Fission Product Transport Model
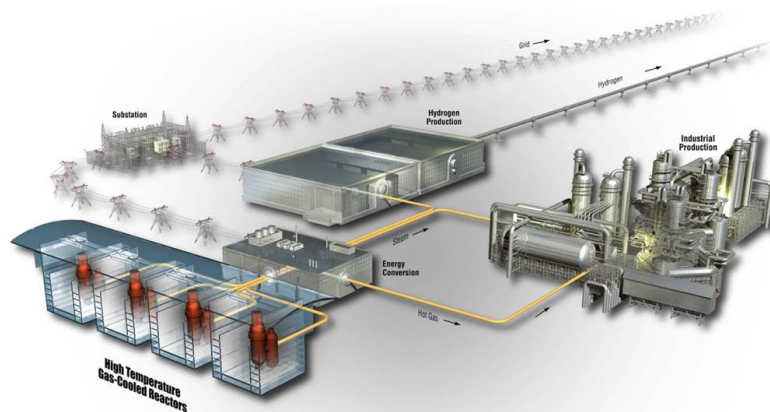
September 2023

Adriaan A. Riet
Idaho National Laboratory

Idaho National Laboratory

Status of Modifications to the AGR-3/4 Fission Product Transport Model

Adriaan A. Riet
Idaho National Laboratory

September 2023

Idaho National Laboratory
Advanced Reactor Technologies
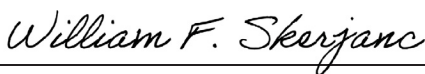**Idaho Falls, Idaho 83415**

http://www.ART.INL.gov

Page intentionally left blank

INL ART Program

Status of Modifications to the AGR-3/4 Fission Product Transport Model

INL/EXT-INL RPT-23-74853
Revision 0

September 2023

Technical Reviewer: (Confirmation of mathematical accuracy, and correctness of data and appropriateness of assumptions.)

William F. Skerjanc   9/25/2023
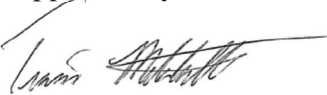
William Skerjanc   Date
ART/AGR TRISO Fuel Performance Modeling
Technical Lead

Approved by:

[signature]   9/25/2023

Travis R. Mitchell   Date
ART Program Manager

Paul Demkowicz   9/26/2023
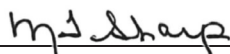
Paul A. Demkowicz   Date
AGR Program Technical Director

[signature]   9/25/2023

Michelle T. Sharp   Date
INL Quality Assurance

Page intentionally left blank

ABSTRACT

A one-dimensional (1D) finite-element model of the AGR 3/4 experiment fission product distributions based on the Multiphysics Object-Oriented Simulation Environment (MOOSE) framework has been revised and implemented within BISON, with improvements which allow for detailed temperature histories to be used for analyses. Empirically determined concentration profiles and ring inventories from the AGR-3/4 experiment have been compiled for comparison purposes. Ongoing efforts to build fission product diffusion models which can describe the applicable physics for isotopic concentration profiles in each AGR-3/4 capsule are discussed, as well as the suitability of each isotopic concentration profile in each capsule for obtaining transport parameters.

Page intentionally left blank

CONTENTS

FIGURES

TABLES

ACRONYMS

1D	one-dimensional
2D	two-dimensional
AGR	Advanced Gas Reactor Program
ATR	Advanced Test Reactor
DTF	designed-to-fail
FB	fuel body
FIMA	fissions per initial metal atom
HTGR	high temperature gas-cooled reactor
IAEA	International Atomic Energy Agency
INL	Idaho National Laboratory
IPyC	pyrolytic carbon (inner layer)
IR	inner ring
MDA	minimum detectable activity
MOOSE	Multiphysics Object-Oriented Simulation Environment
OPyC	pyrolytic carbon (outer layer)
OR	outer ring
ORNL	Oak Ridge National Laboratory
PARFUME	PARticle Fuel ModEl
PGS	precision gamma scanner
PIE	post-irradiation examination
PNNL	Pacific Northwest National Laboratory
R-DLBL	radial deconsolidation leach-burn-leach
SiC	silicon carbide
SR	sink ring
TAVA	time-average-volume-average
TRISO	tristructural isotopic nuclear fuel particle
UCO	uranium oxycarbon

Page intentionally left blank

Status of Modifications to the AGR-3/4 Fission Product Transport Model

1. OVERVIEW

This report details the current and ongoing efforts to model the AGR-3/4 post-irradiation experiment (PIE) results. An overview of the Advanced Gas Reactor (AGR) Fuel Development and Qualification Program, specifically the third and fourth irradiation experiment (AGR-3/4), is described in Section 1. The models used in previous work (Riet and Stempien 2022) have been revised and extended to capture more plausible physical phenomena, and those extensions are discussed in Section 2. Available empirical results for each capsule are summarized and briefly discussed in Section 3. Section 4 contains a brief outline of the models which are currently being developed and how the results of the extended models will be compared to empirical results.

1.1 Overall Program Purpose

The AGR program was established to perform research and development on tristructural isotropic (TRISO)-coated particle fuel to support deploying a high-temperature gas-cooled reactor (HTGR). This work continues as part of the Advanced Reactor Technologies Program. To achieve these goals, the program includes the elements of fuel fabrication, irradiation, PIE of irradiated fuel, post-irradiation heating tests, fuel performance modeling, and fission product transport (INL 2022). Several fuel-irradiation experiments have been performed at the Advanced Test Reactor (ATR) at Idaho National Laboratory (INL 2022), and AGR-5/6/7, the fourth and final irradiation, was completed on July 22, 2020.

1.2 Purpose of AGR-3/4

The AGR-1, AGR-2, and AGR-5/6/7 experiments focused on the performance of high-quality TRISO fuel, and PIE focused on quantifying the probability of silicon carbide (SiC) and TRISO coating failures. In contrast, the AGR-3/4 experiment was primarily a fission product transport experiment focused on observing the migration of fission products throughout the fuel, graphitic matrix material, and nuclear-grade graphites in the presence of exposed fuel kernels (Collin et al. 2018). The experiment consisted of fuel compacts containing TRISO-coated driver-fuel particles similar to AGR-1 baseline fuel (Collin 2015a; Hunn and Lowden 2007; Hunn et al. 2014) and designed-to-fail (DTF) particles that are designed to release fission products during irradiation to migrate through the surrounding cylindrical rings of graphitic matrix and nuclear-grade graphite. Following irradiation, PIE measurements of the fission inventories and spatial distributions (axially and radially) within AGR-3/4 samples (primarily the graphite rings and compacts) were completed (Harp, Stempien, and Demkowicz 2020; Riet 2022; Stempien 2021; Stempien et al. 2018). These data will be used to support refinement of fission product transport models and HTGR source-term analyses.

1.3   AGR-3/4 Fuel Description

A feature of AGR-3/4 fuel that sets it apart from AGR-1 and AGR-2 was the incorporation of 20 DTF particles in each compact in addition to the approximately 1,898 TRISO-coated "driver" fuel particles. DTF fuel kernels were coated only with a thin (20-μm-thick) pyrocarbon layer. This layer was intentionally fabricated with high anisotropy, so it would be likely to fail during the irradiation (Collin 2015a; Hunn and Miller 2009; Kercher et al. 2011), resulting in up to 20 exposed fuel kernels per compact. As shown on the right in Figure 1, the DTF particles (highlighted in red) were aligned roughly along the compact radial centerline. DTF particles provided a known source of fission products to migrate radially outward in the compacts and into the surrounding concentric rings of graphite and/or matrix material. It was expected that intact DTF particles would behave like TRISO particles with SiC layer failures (e.g., releasing substantial Cs but retaining fission gases), and failed DTF particles (DTF particles with breached pyrocarbon layers) would behave like TRISO particles with failed TRISO coatings (e.g., releasing both Cs and fission gases).

The white particles in Figure 1 are the driver particles. AGR-3/4 driver particle fuel kernels were fully TRISO-coated with a buffer layer, inner pyrolytic carbon (IPyC) layer, SiC layer, and outer pyrolytic carbon (OPyC) layer with characteristics similar to the "baseline" variant from the AGR-1 experiment (Collin 2015b; Hunn and Lowden 2007). Both the AGR-3/4 driver and DTF fuel particles contain UCO fuel kernels (approximately 350 μm in diameter) manufactured at BWX Technologies (BWXT) Nuclear Operations Group (Lynchburg, Virginia). The U-235 enrichment was 19.7 wt%. The DTF pyrocarbon coating and the driver-fuel TRISO coatings were applied to the kernels at Oak Ridge National Laboratory (ORNL). Driver particle and DTF particle properties are summarized by Collin (2015a). Complete kernel and particle characterization and fabrication data are compiled in several reports and papers (Hunn and Kercher 2006; Hunn and Lowden 2007; Hunn and Miller 2009; Kercher et al. 2011). Driver-fuel particles and DTF particles had average dimensions, as summarized in Table 1. Particle diameters are more than the sum of the DTF pyrocarbon thickness because an overcoat was used.

AGR-3/4 driver and DTF particles were overcoated with a precursor to graphitic matrix material and formed into cylindrical fuel compacts at ORNL. The compact graphitic matrix material is composed of graphite and a carbonized phenolic resin. Compacts were nominally 12.3-mm in diameter and 12.5-mm long (in contrast to the AGR-1 and AGR-2 compacts, which were approximately 12.3-mm in diameter and 25-mm long). A summary of AGR-3/4 fuel compact properties is provided in the AGR-3/4 Final As-Run Report (Collin 2015b) Detailed characterization data of the as-fabricated compacts were compiled in an ORNL report (Hunn, Trammell, and Montgomery 2011).

In the X-Y compact naming convention, X denotes the capsule number, and Y denotes the level of the compact within the capsule (with level 1 at the bottom and level 4 at the top of the capsule). In AGR-3/4, there were four compacts per capsule. Thus, for example, Compact 3-3 is the third compact from the bottom of Capsule 3, and Compact 12-1 is the bottom compact from Capsule 12.
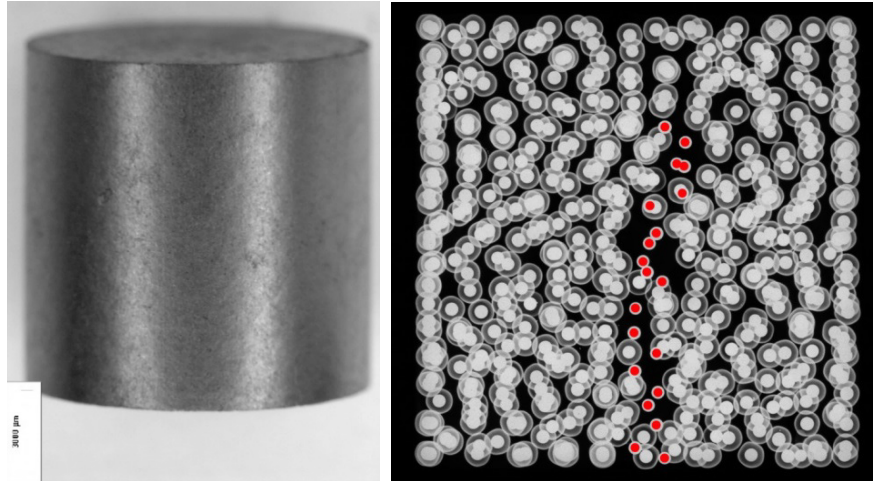
Figure 1. Image of an AGR-3/4 fuel compact (left) and x-ray side view image (right) (Hunn, Trammell, and Montgomery 2011). DTF particles are highlighted with red dots in the x-ray image.

Table 1. As-fabricated particle dimensions and standard deviations from Table A-2 of Collin (2015a).

DTF Particle Properties	
Kernel diameter (μm)	357.3 ± 10.5
DTF pyrocarbon thickness (μm)	20.0 ± 0.9
DTF particle overall diameter (μm)	400.0 ± 9.2
Driver Particle Properties	
Kernel diameter (μm)	357.3 ± 10.5
Buffer thickness (μm)	109.7 ± 7.7
IPyC thickness (μm)	40.4 ± 2.3
SiC thickness (μm)	33.5 ± 1.1
OPyC thickness (μm)	41.3 ± 2.1
Driver particle overall diameter (μm)	818.9 ± 14.2

1.4   AGR-3/4 Test Train, Irradiation, Graphite, and Graphitic Rings

The AGR-3/4 irradiation test train consisted of 12 capsules numbered 1 through 12 from the bottom to the top of the ATR core (Collin et al. 2018). Figure 2 shows a cross section of an AGR-3/4 irradiation capsule. The compacts were stacked vertically in the center of concentric rings made from graphitic matrix material and/or structural graphite (IG-110 and PCEA). Toyo Tanso IG-110 is an isostatically molded graphite with fine grains, and GrafTech PCEA is an extruded graphite. The matrix rings were produced at ORNL using a recipe similar to the historic German A3-27 formulation (Hunn, Trammell, and Montgomery 2011). These matrix rings were fabricated with a blend of natural and synthetic graphite flake mixed with Hexion SD-1708 novolac resin. BWXT provided this blend of graphite flake and resin to ORNL.
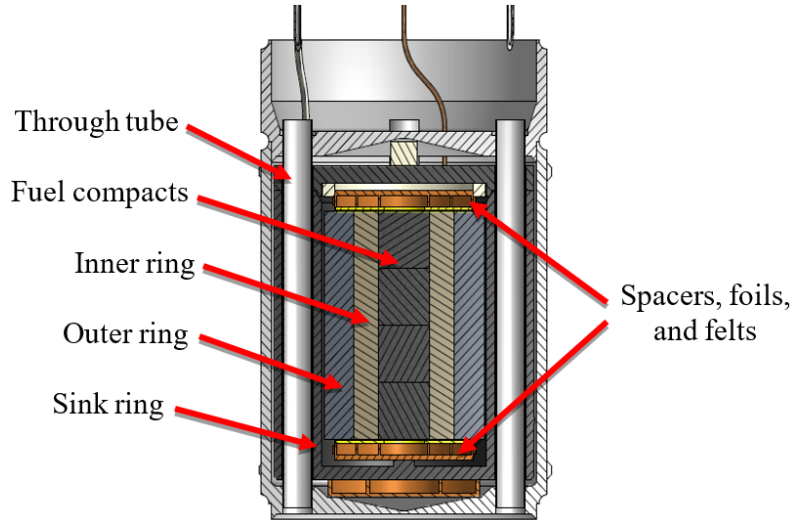
Figure 2. Axial cutaway diagram of a standard AGR-3/4 irradiation capsule.

Table 2 lists the materials, types of capsules, and PIE measurement diameters for each ring. There were two types of capsules: "standard" and "fuel body" (FB). The standard capsule type is depicted in Figure 2 where the outer ring (OR) is open on its top and bottom. Fuel bodies, on the other hand, had floors and a lid that screwed on to the top of the OR. Each capsule also included several small spacers of various materials (graphite, zirconia, or zircaloy-4) and graphite foils to separate components and act as thermal barriers to control temperature in the compacts. Compact lengths were measured as part of PIE, but ring lengths were not measured. All inner rings (IRs) had as-fabricated lengths of 50.8 mm (2.0 in.). In standard capsules, OR lengths were 50.8 mm (2.0 in.). In fuel bodies, the ORs had a sealed bottom and a lid for a total overall length of about 61.0 mm (2.4 in.). Sink ring (SR) lengths were generally about 63.5 mm (2.5 in.); however, some SRs were about 71.1-mm (2.8-in.) long. All SRs had lids and sealed bottoms. SRs had relatively cold irradiation temperatures (typically 500–600°C) to stop further radial transport of fission products during the experiment.

Table 2. AGR-3/4 capsule types, ring materials, and ring dimensions from PIE (Stempien et al. 2016). Complete sets of dimensions and uncertainties are available in Stempien (et al. 2016).

Capsule No.	Capsule Type	Ring Material			IR Diameters (mm)		OR Diameters (mm)		SR Diameters (mm)	
		Inner	Outer	Sink	ID	OD	ID	OD	ID	OD
1	Std	Matrix	PCEA	PCEA	12.55	23.61	24.53	33.50	41.21	61.59
2	FB	Matrix	PCEA	PCEA	N/A	N/A	N/A	36.72	39.33	62.05
3	Std	PCEA	PCEA	PCEA	12.62	24.03	24.86	33.08	41.42	63.56
4	FB	Matrix	PCEA	PCEA	12.71	23.87	24.70	39.24	39.48	63.32
5	Std	Matrix	PCEA	PCEA	12.67	23.89	24.68	39.39	39.54	63.61
6	FB	Matrix	PCEA	PCEA	N/A	N/A	N/A	39.33	39.48	63.30
7	Std	Matrix	PCEA	PCEA	12.75	23.67	24.93	37.35	39.53	63.63
8	Std	IG-110	IG-110	PCEA	12.60	24.07	24.77	38.55	39.57	63.64
9	FB	Matrix	IG-110	PCEA	N/A	N/A	N/A	39.27	39.46	63.08

Capsule No.	Capsule Type	Ring Material			IR Diameters (mm)		OR Diameters (mm)		SR Diameters (mm)	
		Inner	Outer	Sink	ID	OD	ID	OD	ID	OD
10	Std	PCEA	PCEA	PCEA	12.58	24.04	24.83	37.48	39.40	63.43
11	FB	Matrix	PCEA	PCEA	N/A	N/A	N/A	33.29	N/A	N/A
12	Std	Matrix	PCEA	PCEA	12.47	24.23	24.51	34.98	39.34	61.60
Std: standard capsule										
N/A: not available										

2. METHODS

2.1 Inventory Analysis

To determine the fission product mass balance, each of the 12 irradiation capsules was disassembled, and their component parts were analyzed via gamma spectrometry, mass spectrometry, and gas proportional counting (Stempien et al. 2018). The most commonly detected radionuclides were gamma-emitting Ag-110m, Cs-134, Cs-137, Eu-154, Eu-155, and beta-emitting Sr-90. In standard capsules (Capsules 1, 3–5, 7–8, 10, and 12), IR, OR, SRs, spacers, foils, felts, and through tubes were all analyzed. The metallic hardware was acid leached, and that leachate was analyzed for gamma-emitting nuclides and Sr-90. Small non-metallic hardware (e.g., spacers, foils, and felts) and the large graphite SRs were gamma counted using common high-purity germanium detectors before leaching (of ceramic spacers) or burn-leaching (of carbonaceous samples like felts and SRs) was performed to allow measurement of Sr-90 in the leachate.

The precision gamma scanner (PGS) was used to measure the inventory of gamma-emitting fission products in the compacts and IRs and ORs (Harp, Stempien, and Demkowicz 2020). Select rings were also subjected to tomographic gamma scans on the PGS, and subsequent tomographic reconstructions of those scans was used to produce 1D radial and 2D representations of the fission product spatial distributions in the rings (Riet 2022). In addition to non-destructive gamma spectrometry of entire rings, portions of the IRs and ORs from Capsules 3, 5, 7, 8, 10 and 12 were destructively analyzed for both gamma-emitting nuclides and beta-emitting Sr-90 (Stempien 2021) (see Section 2.2). FB Capsules 2, 6, 9, and 11 were retained intact for heating tests; thus, the compacts, smaller non-metallic items (e.g., spacers), and IR and ORs from these capsules were not measured.

Summing the fission product inventory measured on each capsule component made it clear that the presence of 80 DTF particles in each capsule resulted in noticeably higher releases of cesium (Cs-134 and Cs-137) from AGR-3/4 fuel when compared to AGR-1 and AGR-2 fuel, which did not have DTF particles. Greater than 30 particles' worth of cesium was measured outside of the fuel compacts in Capsules 3-5, 7, 8, and 10. In Capsule 11 (an intact FB for which the IRs and ORs were not measured), 26 particle equivalents of cesium were measured outside of the OR. Based on experience from AGR-1, it is very unlikely that any driver particles failed during the irradiation (Demkowicz et al. 2015); therefore, this cesium is assumed to be overwhelmingly dominated by release from DTF particles (Stempien et al. 2018).

Higher levels of europium and strontium release were also observed in AGR-3/4 when compared to AGR-1, and when compared to most capsules from AGR-2. Tens of particles worth of Eu-154 or Eu-155 were typically measured outside of the fuel compacts (even in the FB capsules for which the mass balance is incomplete). This is largely due to the DTF particles.

When analysis of the data from physical sampling of portions of the IRs and ORs of Capsules 3, 4, 7, 8, and 10 was completed, a Sr-90 balance for the entirety of those rings was estimated and added to the Sr-90 balance contributed from other components of those capsules (e.g., spacers, foils, and metallic hardware). Currently, the estimated AGR-3/4 Sr-90 balances give one to two orders of magnitude higher release than the entire in-pile Sr-90 releases from AGR-1. As in the case of europium, this is due substantially to the DTF particles. More details can be found in INL/EXT-18-46049 (Stempien et al. 2018).

2.2   Physical Sampling

Physical sampling of the rings involved milling material from around the circumference of the rings, collecting that material, and analyzing it for gamma-emitting fission products and beta-emitting Sr-90. The fines from milling each step were collected in individual vials, and those were sent to Pacific Northwest National Laboratory (PNNL) where they were gamma counted for key isotopes such as Ag-110m, Cs-134, Cs-137, Ce-144, Eu-154, and Eu-155. After gamma counting the solid samples (i.e., the fines from milling), the samples were transferred to fused silica beakers and oxidized in a muffle furnace at 750°C for 24 hours. The ash and residue remaining in the beaker was dissolved with HNO_3. In instances where solids did not dissolve using only HNO_3, small amounts of concentrated HF in HNO_3 were used. PNNL reported that solutions with residual solids were centrifuged, the supernate was decanted, and HF and HNO_3 were added. This process was repeated until all solids were dissolved. All the solutions for a given sample were combined. A Sr-90 separation process using an Eichrom strontium resin was then performed for the solutions. After the Sr-90 separation, Sr-90 was quantified by liquid scintillation counting. Knowing the thickness and location of material removed from the ring in each milling step and the fission product inventory in the material collected from each milling step, the radial fission product concentration profiles in the rings were constructed. Further details can be found in INL/EXT-21-62863 (Stempien 2021).

2.3   Fuel Compact Radial Deconsolidation

Selected fuel compacts have been subjected to electrolytic radial deconsolidation-leach-burn-leach (R-DLBL) (Stempien 2017). Radial deconsolidation sequentially removes radial segments of compacts from the outside-in so that each segment can be analyzed separately for fission products and a fission product concentration profile can be constructed. In regions of the compact away from the DTF particles, this method gives the fission product inventory in the fuel compact matrix and the OPyC of the driver-fuel particles. In the central region of the compact, where the DTF particles reside, this method gives the fission product inventory retained in the DTF particles, plus that in the fuel compact matrix, and the OPyC of driver-fuel particles surrounding the DTF particles. Some reports detailing the radial deconsolidation work are complete (Hunn et al. 2020; Helmreich et al. 2021 and 2022), others are in progress with preliminary results included here.

2.4   One-Dimensional Finite-Element Method Model

Starting with the work described in (Riet and Stempien 2022), transport of fission products through the rings in each capsule was modeled using the BISON code in the Multiphysics Object-Oriented Simulation Environment (MOOSE) finite-element framework (Lindsay et al. 2022; Williamson et al. 2021). The capsule dimensions were obtained from post-irradiation metrology (Stempien et al. 2016) where available. Where post-irradiation metrology was not available, dimensions were taken from capsule design documents. The finite-element model simplifies the design of the experiment to a 1D radially symmetric transport problem, as shown in Figure 3, with the center of the capsule on the left and the outer surface of the graphite SR on the right. The DTF region and driver particle region are modeled as homogenous volumes with a defined source term. Gas gaps are modeled explicitly.
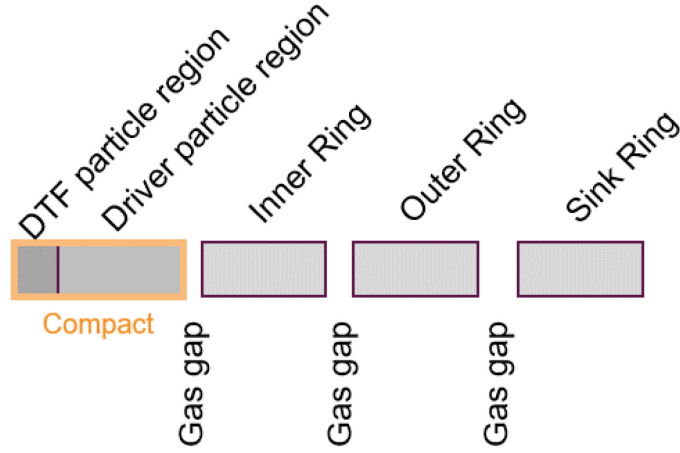
Figure 3. Geometry of the finite-element model.

The finite-element mesh was generated for each region in Figure 3 with uniformly spaced meshes in each region. To ensure stability, the total number of mesh elements in each region was adjusted such that the inequality (1) was satisfied for all elements in the simulation. This was a change from the previous work, as the process to specify a weighted sigmoid distribution function interferes with the capacity of BISON to apply adaptive mesh refinement.

$$\min\left(\frac{D_0 \exp\left(-\frac{E_a}{RT(x)}\right)}{\Delta x^2}\right) > 1 \tag{1}$$

Transport into the gas gaps was accounted for using the Freundlich isotherm (2), where P_{gas} is the vapor-phase pressure in pascals, C_{int} is the concentration of the isotope at the interface in mol/m^3, ρ is the density of the graphite material in g/cm3 (this converts the concentration to mmol/kg carbon, which are the units in which the isotherm correlation is derived) and A, B, D, E, d_1, and d_2 are experimentally determined. The values of the experimentally determined constants are material dependent, and those used previously are listed in Table 3.

$$P_{gas} = \begin{cases} \frac{C_{int}}{\rho} \exp\left(\left(A + \frac{B}{T}\right) + \left(D - 1 + \frac{E}{T}\right)(d_1 - d_2 T)\right), & C_{int} < (d_1 - d_2 T) \\ \left(\frac{C_{int}}{\rho}\right)^{D + \frac{E}{T}} \exp\left(A + \frac{B}{T}\right), & C_{int} > (d_1 - d_2 T) \end{cases} \tag{2}$$

Table 3. Historical Freundlich isotherm parameters.

	Material Measured	Used to Model	A	B [K]	D	E [K]	d_1	d_2 [1/K]	Reference
Ag	NBG-17	Matrix & Graphite	60.7	-78479	-7.268	9362.1	-20.11	-0.0227	Fit to data (Walton et al. 2021)
Cs	Fuel rod Matrix Material (Ashland A-240)	Matrix	19.3	-47300	1.51	4340	3.4	6.15×10^{-4}	(Myers, et al., 1979)
Cs	Unirradiated H-451	Graphite	24	-35700	-1.56	6120	2.04	1.79×10^{-3}	(Myers, et al., 1979)
Sr	Fuel compact matrix material[a]	Matrix	54.3	-149000	-8.52	28500	3.13	0	(IAEA 1997)
Sr	H-451 and H-327	Graphite	19.4	-40100	-0.32	4090	-2.12	0	(Myers, et al., 1974)

Many of the values in Table 3 were determined from historical nuclear graphites, so they may vary somewhat from the properties of modern graphites (for example: IG-110, PCEA, NBG-17). There are no experimentally determined values for silver sorption on matrix material; therefore, NBG-17 graphite parameters extracted from Walton et al. (2021) were used. As the model provided in the literature for silver was obtained in a limited temperature range and concentrations well above those observed here, the parameters obtained provided nonphysical results for these conditions. Instead of using the parameters as derived by Walton et al. (2021), a bounded regression was used to estimate model parameters which are shown in Table 3, though the regression obtained is not of high confidence.

The source terms for the model in the DTF and driver regions were obtained using PARticle Fuel ModEl (PARFUME) particle release calculations (Skerjanc 2016). As an input to PARFUME, and for the DTF particle releases, total production of fission products was calculated using as-run coupled neutronics and depletion models (Sterbentz 2015). The boundary conditions on the center of the compact and on the outside of the SR are both insulating (i.e., Neumann) boundary conditions with transport across the boundary set to zero. A zero-concentration boundary condition was also investigated on the outside of the SR, and no practical difference was observed between the two.

---

[a] "The fuel compact matrix material is not a matrix graphite but a combination of fired carbonaceous material, graphite grains, and coated fuel particles. The transport of condensable fission products will be mainly on the surfaces of the carbonaceous material The release of condensable fission products from the compact is by desorption, homogeneous concentration within compact." (IAEA 1997)

In contrast to (Riet and Stempien 2022), where there was a time-averaged temperature boundary condition, in this work, time-dependent temperature boundary conditions at the inner and outer edges of each ring are calculated from the ABAQUS models used to generate the as-run thermal report (Hawkes 2016). Average temperatures of the ring edges are applied as boundary conditions with time spent at very low temperatures (room temperature offline conditions) omitted for sake of computational efficiency. This change was possible due to structural changes in the numerical model when the sorption model was incorporated into BISON.

An additional benefit of the model implementation in BISON is the flexibility to use alternate sorption isotherm models. Given the very low (ppm) concentration measurements of fission products, it is unlikely that there is interaction between fission products at the graphite or matrix surfaces, and a simple Henrian sorption model will likely suffice to capture the relevant physics. Furthermore, as only the ratio of sorptivity across the gap influences the solid-phase concentrations measured (Humrickhouse et al. 2016), only a single parameter describing the temperature-dependence of the sorptivity is needed. Model parameters are in the process of being fit to the measured data shown in this report through an inverse process using a constrained-trust region optimization routine in the scipy python package. In fitting, we assume an Arrhenius form of the sorption temperature dependence and derive a best-fit model of diffusivity and sorptivity concurrently.

2.5   Two-Dimensional Finite Element Model

In addition to the one-dimensional model described in Section 2.4, a new two-dimensional axially symmetric model was constructed to evaluate the potential for fast transport "short-circuit" diffusion paths through small gas gaps above and below the rings, as shown in Figure 4. To account for potential two-dimensional effects, each physically sampled region is distinctly labeled and can be compared individually. The model is explicitly meshed in the gas-gap regions, though as of this writing, gas-gap transport is modeled without convective effects and a constant diffusivity of 10^{-7} m^2/s. The ABAQUS models used to generate the as-run thermal report (Hawkes 2016) were utilized to obtain time-dependent temperature profiles as a function of axial height at each capsule boundary, with heat conduction modeled between the surfaces to obtain a consistent time-dependent temperature profile across the simulation domain.

Though a more thorough ongoing study will evaluate the potential for correlation-based buoyancy-driven convective transport, preliminary modeling shows that gas-gap transport provides a smooth decreasing gradient in concentration on the edge of the capsule contacting the gas-gap. Thus, the primary mechanism by which an increase in observed concentration at the outer edge of a ring would be consistent with this model is slower diffusion through the bulk with very high surface concentrations on all edges which would diffuse inward on all sides. In all cases using these physics, the concentrations measured at the edge of the ring should be greater than the concentration profiles measured at the center of the ring. It should be noted that the SR is taller than the other rings in the physical capsules than in the model. Consequently, the modeled gas gap above and below the SR is inconsistent with reality and will be removed in future iterations.
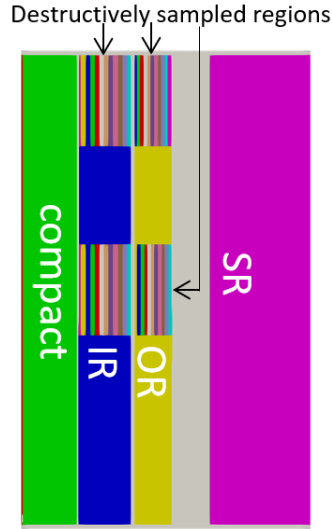
Figure 4. Two-dimensional model geometry of Capsule 3, with the DTF region on left and SR on far right. Gas gaps between rings are in gray, and each physically sampled region is distinctly categorized. The driver particle region is in green, with un-sampled sections of the IR and OR in blue and yellow respectively. The SR is magenta. The physically sampled areas are striped bands.

3. COMPILED FISSION PRODUCT DISTRIBUTION RESULTS

The AGR-3/4 fission product transport model results were compared to measured fission product inventories and spatial distributions for each capsule in the experiment. There are three primary types of measurements obtained in PIE to be compared against:

1. Total radionuclide inventories – Totals measured outside of the fuel compacts and total inventory in individual parts of the test such as the inner, outer, and SRs.

2. Spatial radionuclide concentrations – Gamma tomography provided 2D maps of gamma-emitter distributions at specific axial locations in the IRs and ORs. These have also been used to construct radial fission product concentration profiles. Destructive sampling of selected IRs and ORs has produced radial fission product concentration profiles for both gamma-emitting nuclides and Sr-90. In some cases, rings were sampled at multiple axial locations (Stempien 2021). These are represented by square ■ or star ☆ markers. On some ORs, small "nubs," protrusions on the surface intended to aid in centering the ring in the cavity, were large enough that a separate sample of fission product concentration was taken at the nubs (see Figure 5). These are shown where available and are represented by filled diamond ◊ markers. Nubs were features exclusive to the top and bottom outer surface of the rings, so some inconsistency corresponding to the difference in axial location may be expected.

3. Radionuclide inventories in fuel compacts – Selected AGR-3/4 fuel compacts were subjected to R-DLBL, which gives fission product concentrations in the compact matrix outside the SiC layer of the TRISO-coated driver-fuel as a function of radius in the compact. As there is no SiC layer in the DTF particles, radial deconsolidation of the core of the compact (highlighted red region in Figure 1) yields the entire residual inventory of the DTF particles. The R-DLBL segmented the compact into several 0.5-3 mm thick (diameter reduction) circumferential sections before taking the remaining roughly 6 mm together as the compact core, though there were occasionally complications leaving a larger diameter core. Additionally, some driver particles were broken during the deconsolidation process; where possible, the magnitude of their inventory was subtracted from the measured values before being included here. A detailed description of the methods used to calculate the radii of R-DLBL samples has been provided previously (Stempien 2017).
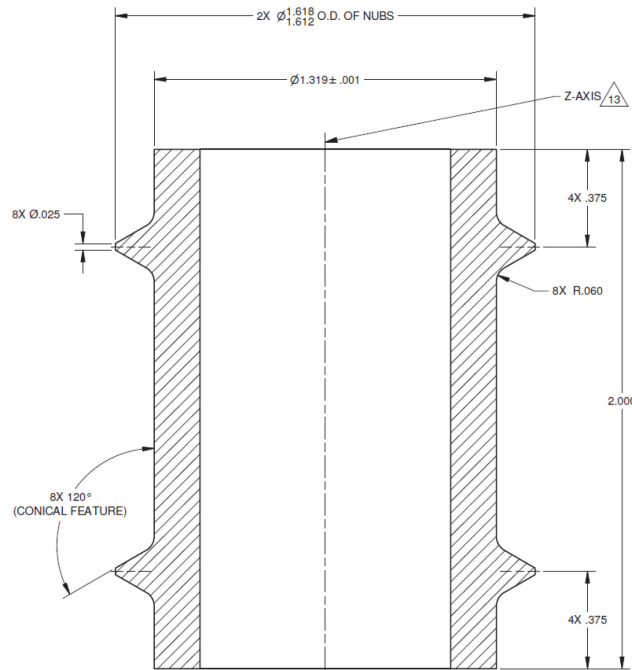

Figure 5: Cross-sectional drawing of the Capsule 3 OR (INL 2011). Conical protrusions are here referred to as "nubs."

Figure 7–Figure 54 depict the results of the measurements which will be used as ground-truth to benchmark the models described in Sections 2.4 and 2.5. Most of the measurements correspond to a concentration profile, with the exception of the total ring inventory from the mass-balance report measurements (denoted by a filled circle ● or +) (Stempien et al. 2018) as both show the average concentration for a given ring. Concentrations obtained from R-DLBL measurements are shown only where the compact was analyzed in the as-irradiated state, and are denoted by a triangle located at the center of the measured region with error bars extending to the radial extent of the measurement. When the models described in Sections 2.4 and 2.5 are fit to data from the compacts, the measurement of the core in the compact which includes the DTF particle inventory is discarded. In some cases, the measurement of a particular isotope's concentration yielded a result not statistically distinct from zero. For these measurements, an open symbol is shown, denoting the minimum detectable activity (MDA) of that isotope. As such, open symbols denote only an upper bound on the concentration. Because the transport calculations were performed in terms of elements, and the measurements quantified specific isotopes, the isotopic measurements are scaled to the modeled overall elemental concentrations using as-calculated isotopic abundances for the two compacts in the center of each capsule. Isotopic abundances were obtained from Sterbentz (2015). This allows for direct comparisons between the modeled results and the measurement results. For reference, the time-average temperature of the compact, and of each ring as modeled is provided across the top of Figure 6–Figure 54. Figure 6 shows the general layout of Figure 7–Figure 54. For reference, a concentration of 1 mol/m^3 in a graphite of density 1.86 g/cm^3 is approximately 6.5 parts per million by mole. The concentrations shown in the profiles are derived from the decay-corrected total activity measurement and the estimated volume of each sample. For reference, capsule rings, materials and associated analyses performed are shown in Table 4.

Table 4. Summary of capsule types, ring materials and analyses performed.

| Capsule	Type	Ring Material		Axial PGS		PGS Tomography		Physical Sampling	
		Inner	Outer	Inner	Outer	Inner	Outer	Inner	Outer
1	Std	Matrix	PCEA	Y	Y	N	N	N	N
2	FB	Matrix	PCEA	N	N	N	N	N	N
3	Std	PCEA	PCEA	Y	Y	Top and Center	Center	Top and Center	Top and Center
4	FB	Matrix	PCEA	Y	Y	Center	N	Top, Center and Bottom	Center and Bottom
5	Std	Matrix	PCEA	Y	Y	Center	N	Center	Center
6	FB	Matrix	PCEA	N	N	N	N	N	N
7	Std	Matrix	PCEA	Y	Y	Center	Center	Top and Center	Top and Center
8	Std	IG-110	IG-110	Y	Y	Top and Center	Center	Center and Bottom	Center and Bottom
9	FB	Matrix	IG-110	N	N	N	N	N	N
10	Std	PCEA	PCEA	Y	Y	Top and Center	N	Center and Bottom	Center and Bottom
11	FB	Matrix	PCEA	N	N	N	N	N	N
12	Std	Matrix	PCEA	Y	Y	N	N	Center and Bottom	Center and Bottom

Y: yes
N: no
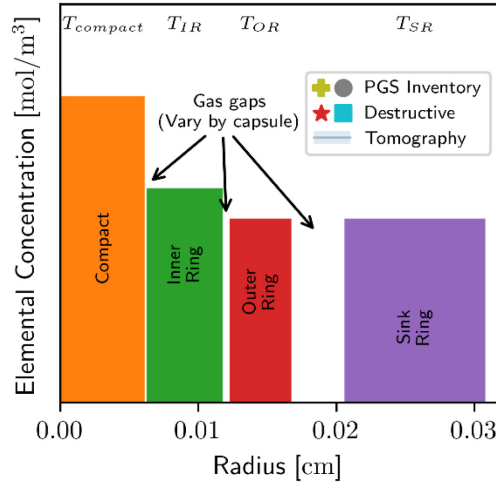
Figure 6. General layout of results given in Figure 7–Figure 54. A representative time-weighted average temperature across all of the compacts or each ring are shown on the top of the figure, derived from the as-run thermal analysis (Hawkes 2016). Tomographic reconstruction data are semi-transparent, and where multiple tomographic measurements of the same ring are available (such as when two different axial locations on the same ring were scanned), a filled region between all tomographic concentration estimates is shown.

3.1 Isotope Overviews

3.1.1 Cesium

Cesium has two isotopes which generally yield high-quality measurements after a decay time of a few years, ^{134}Cs and ^{137}Cs. The ^{134}Cs isotope has a half-life of about 2 years and as such measurements of ^{134}Cs are generally considered more reliable as it has a more limited potential to be confounded with hot-cell contamination than ^{137}Cs with a half-life of 30 years.

Measured concentrations of cesium generally decrease radially within the compact and IRs, though not without exceptions. OR concentration profiles are more complicated, and as the activities are lower, generally suffer from worse counting statistics, though it should be noted that very few measurements of cesium activity fell below the MDA. There is some indication that literature parameters predict a higher activation energy for cesium transport than is observed in this data set; we observe both faster transport at lower temperatures and slower transport at high temperatures than is predicted by radial diffusion models based on the existing collection of diffusivities and sorptivities (IAEA 1997).

3.1.2 Silver-110m

The metastable ^{110m}Ag has a half-life of 249 days. Silver-graphite transport between 1000–1200°C is complex. A sessile drop of silver resting on a graphite surface interacts strongly enough to change the surface morphology in tens of minutes (Pittoni, Chang, and Lin 2012), and silver transport at 1000°C is fast. The measured silver concentration profiles in the rings reflect this complexity. The concentration profiles do not seem to follow a diffusion-dominated process at all, though the expected decrease in silver concentration is observed across rings. Attempts to measure silver during fuel compact radial deconsolidations were made, but any ^{110m}Ag was below the MDA.

3.1.3   Strontium-90

Unlike gamma-emitters, ^{90}Sr required destructive methods for measurement. The total inventories of the SRs were determined via burn-leach (Stempien et al. 2018). Azimuthally-averaged radial concentration profiles were obtained for ^{90}Sr via destructive sampling of portions of IRs and ORs (Stempien 2021). Total ^{90}Sr inventories for these rings have been estimated (Stempien 2021), but are not shown here. Strontium concentrations from R-DLBL of the compacts are consistent with radial outward diffusion, though the IR and ORs exhibit increased concentrations at their edges. Furthermore, some concentration profiles, such as that of the centerline in Capsule 10 shown in Figure 45, are more consistent with a temperature-dependent solubility profile than a diffusion profile. As ^{90}Sr has a gaseous precursor, ^{90}Kr with a half-life of 32 seconds, there may be small amounts of ^{90}Sr that have permeated throughout the rings as ^{90}Kr before decaying, so it may be that not all measured ^{90}Sr activity is indicative of ^{90}Sr transport.

3.1.4   Europium-154

Published diffusivities, sorptivities, and surface kinetics parameters are not available for ^{154}Eu transport through all the TRISO particle layers, so historically it has been assumed to transport through TRISO in a similar fashion to strontium. This is supported by observations from PIE and safety testing from the AGR experiments, which indicate qualitatively similar release behavior for Eu and Sr with slightly higher overall release fractions for Eu. There are several measured concentration profiles of europium that are complex, though it may be possible to fit the concentration gradients at the inner and outer edges of the rings and compacts to a radial diffusion model. This should be done with caution, as not all compact profiles are sufficiently explained by the implicit assumptions in a diffusion model. Additionally, understanding the sorption activity of europium is critical, as the currently assumed sorption model (Riet and Stempien 2022) does not sufficiently capture the observed release from the compacts.

3.2   Capsule Details

3.2.1   Capsule 1

The four Capsule 1 compacts had burnups ranging from 5.43 to 6.85% fissions per initial metal atom (FIMA), with compact fast neutron fluences of 1.42–2.10 (10^{25} n/m^2, E > 0.18 MeV) at the end of irradiation (Collin et al. 2018). The time-average peak temperature within the compacts was 978°C. The time-average-volume-average (TAVA) temperature of the compacts, inner, outer, and SRs were 927, 853, 765, and 517°C, respectively (Hawkes 2016). The calculated axial variation in temperature was less than 131°C for the compacts[b] (see footnote), 82°C for the IR and 28°C for the OR. Capsule 1 is a standard capsule, with a graphitic matrix IR, PCEA OR, and PCEA SR. No tomographic reconstructions were performed on Capsule 1.

Capsule 1 has not had any destructive sampling for the rings, but radial deconsolidation of compacts 1-3 and 1-4 was completed. The results seem to be consistent, with decreasing concentrations in each successive ring starting with the compact, when compared with measurements from (Stempien et al. 2018).

---

[b]   The axial temperature difference is across all four compacts, and was calculated from Figures 56–67 of Hawkes (2016). It was estimated by taking the largest maximum difference in temperature at each radial position for each cycle-average temperature distribution. The largest of the maximum differences is reported here.

Cesium concentration profiles of the compact and IR have been fit to a 1-D Fickian diffusion model with a Henrian sorption isotherm, as shown in Figure 7. As discussed by Humrickhouse et al. (2016), only the ratio of sorptivity as a function of temperature factors into the diffusion model. Based on this fit, we calculate the average diffusivity of the compact, IR, OR and SR to be 2.8×10^{-13} m^2/s, 7.9×10^{-13} m^2/s, 1.1×10^{-14} m^2/s and 1.5×10^{-17} m^2/s. The derived activation energy of the Henrian sorption isotherm is 1.56×10^4 K^{-1}. The fit was not constrained by the measured OR and SR inventories, and significantly underpredicts cesium activity in those rings.

Silver, shown in Figure 8, was not present in quantities above the MDA in the compact radial DLBLs and IR and OR. The total inventory retained in the SR will be useful in verifying the overall results of the model. Literature models overestimate the release of silver for Capsule 1 by just over a factor of 10 (Riet and Stempien 2022).

Strontium's compact concentration profile shown in Figure 9 is difficult to reconcile with the average SR concentration, which may be especially useful in constraining the activation energy of strontium diffusion in graphite and matrix material, but may require an assumption that everything leaving the compact is in contact with all of the rings simultaneously.

Europium transport is relatively straightforward to calculate in Capsule 1 as the only available data (Figure 10) are for the compacts and IR. Although this is the case, the IR inventory is too large to be compatible with the sorption isotherm for strontium, which was assumed previously, and as such the primary utility of the IR inventory is to constrain the ratio of europium sorptivity across the gap.
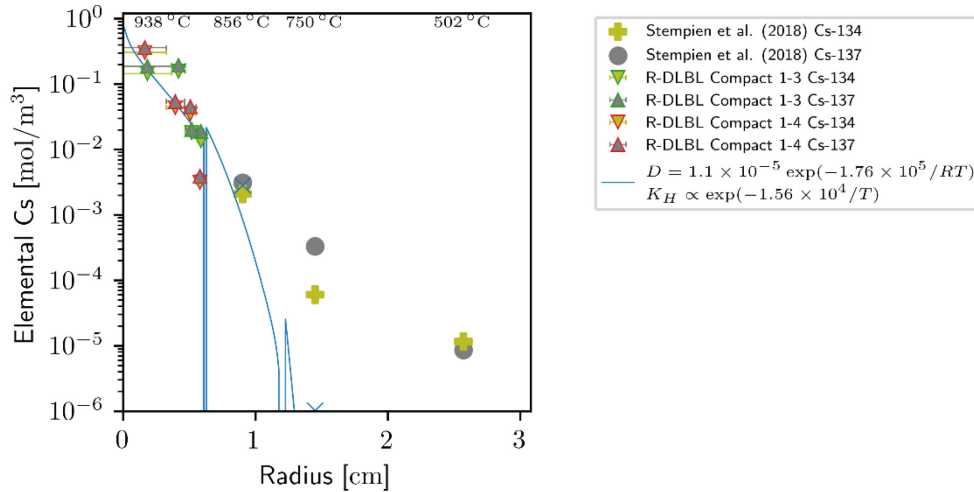

Figure 7. Capsule 1 cesium compact concentration profile, overall ring concentrations and best-fit one-dimensional diffusion model.
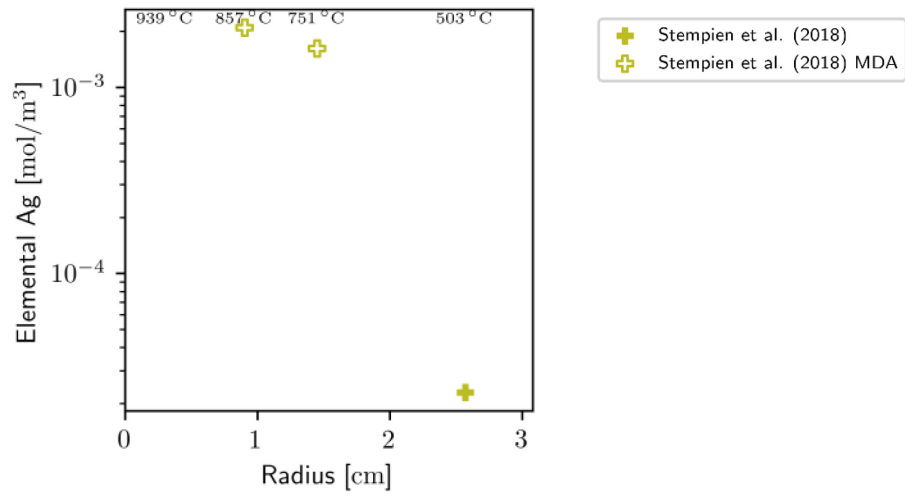
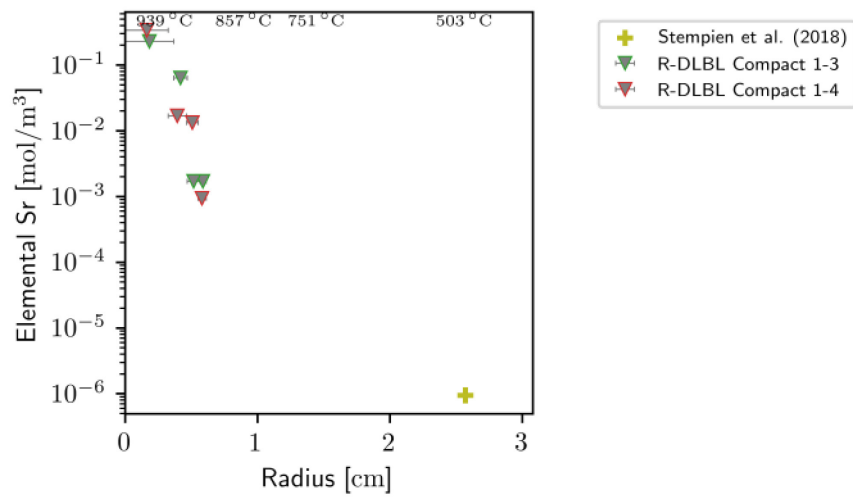Figure 8. Capsule 1 silver overall ring concentrations.

Figure 9. Capsule 1 strontium compact concentration profile and overall ring concentrations.
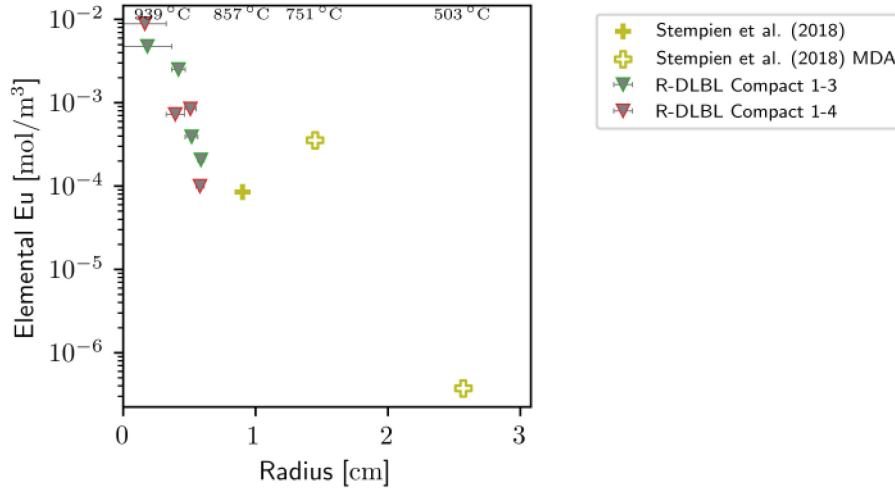
Figure 10. Capsule 1 europium compact concentration profile and overall ring concentrations.

3.2.2 Capsule 2

Capsule 2 was an FB capsule with a matrix IR and PCEA outer and SRs. The OR of this FB was not opened; thus, only the SR and some capsule internals were measured for fission products. Capsule 2 had compact burnups of 9.43–10.65% FIMA, with compact fast neutron fluences of 2.95–3.44 (10^{25} n/m², E > 0.18 MeV) at the end of irradiation (Collin et al. 2018). The time-average peak temperature within the compacts was 1113℃. The TAVA temperatures of the compacts, inner, outer and SRs were 1057, 934, 859, and 609℃ respectively (Hawkes 2016), and the calculated axial variation in temperature was less than 116℃ for the compacts, 50℃ for the IR, and 30℃ for the OR. Capsule 2 has been retained for other analyses. The SR overall concentrations shown in Figure 11–Figure 14 will primarily be used to verify the results of model fitting done on other capsules.
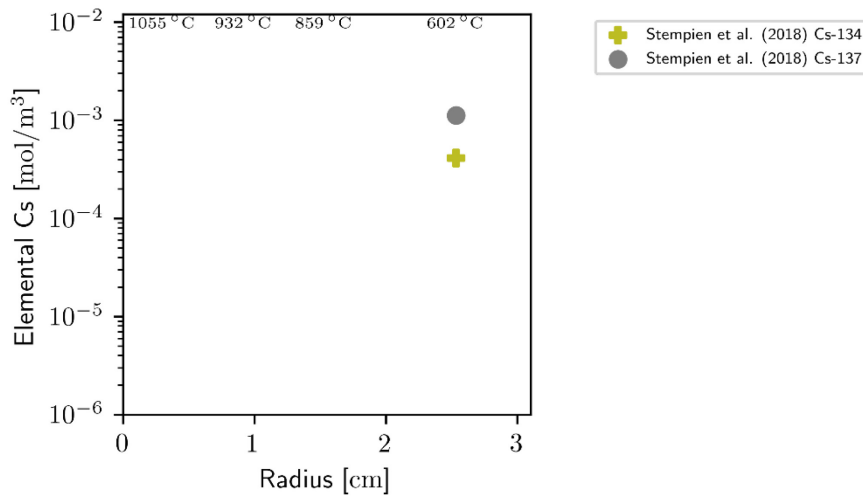

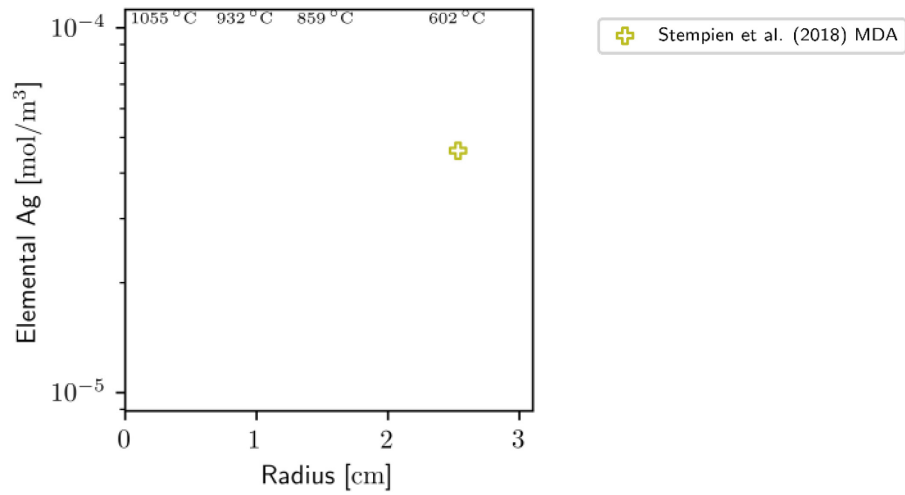Figure 11. Capsule 2 cesium SR concentrations.

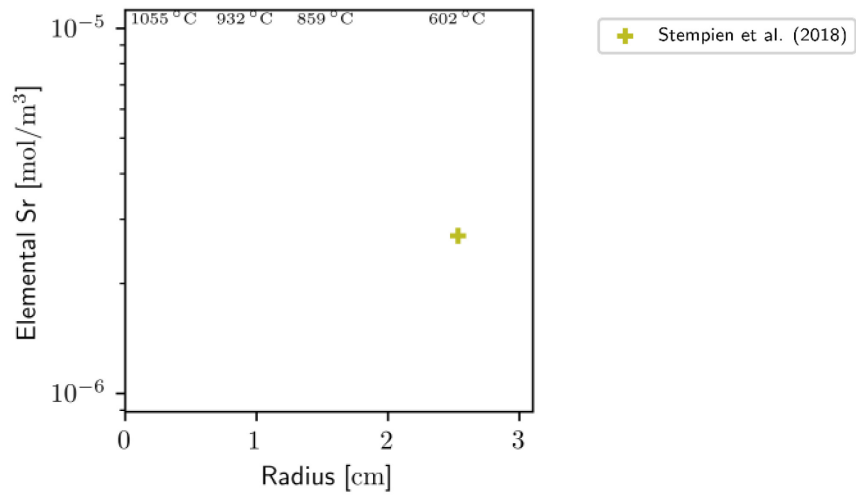Figure 12. Capsule 2 silver SR MDA concentration.
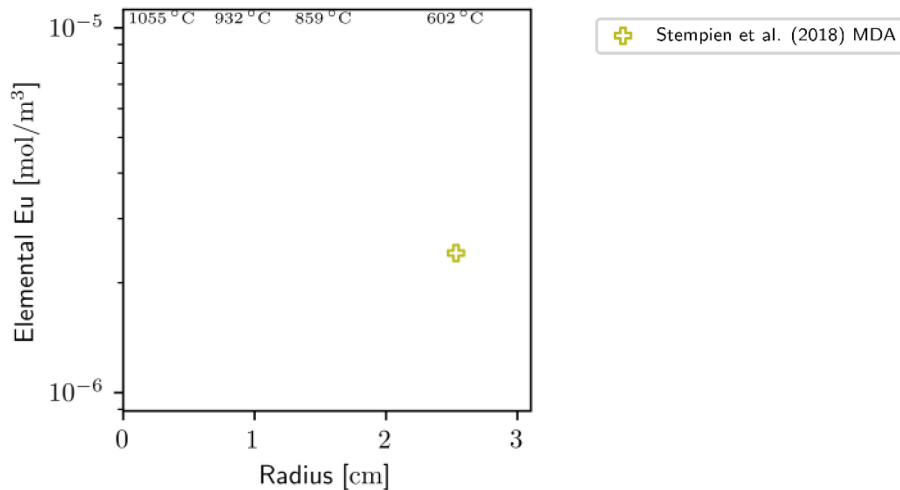

Figure 13. Capsule 2 strontium SR concentration.

Figure 14. Capsule 2 europium SR MDA concentration.

3.2.3 Capsule 3

Capsule 3 is a standard capsule, and all the Capsule 3 rings were made from PCEA. Capsule 3 had compact burnups of 12.16–12.93% FIMA, with compact fast neutron fluences of 4.04–4.38 (10^{25} n/m^2, E > 0.18 MeV) at the end of irradiation (Collin et al. 2018). The time-average peak temperature within the compacts was 1242°C. The TAVA temperatures of the compacts, inner, outer, and SRs were 1177, 1026, 962, and 539°C, respectively (Hawkes 2016). The calculated time-averaged axial variation in temperature was less than 177°C for the compacts, 54°C for the IR, and 24°C for the OR. The IR and OR of Capsule 3 were subjected to destructive physical sampling to generate radial fission product concentration profiles (Stempien 2021). These data points are included here using star and square symbols in the following plots. R-DLBL of Compact 3-2 was also performed and is the subject of a forthcoming INL report. The relevant data are shown here as triangles.

In addition to having multiple sections of the IR and OR sampled destructively, radial deconsolidation of the compact and tomographic scans were taken at multiple elevations in Capsule 3. The resulting concentration profiles for the compact and IR are detailed, with high enough concentrations that very few measurements were below the minimum detectable activity.

Cesium concentration profiles in Capsule 3 shown in Figure 15 are consistent with diffusion radially outward, though the OR in this case exhibits signs of other processes at work. When modeled using every available set of literature transport parameters (IAEA 1997), the predicted inner, outer, and SR inventories agree within a factor of 10, so current models may be sufficient to describe the results.

Silver concentration measurements in Capsule 3 shown in Figure 16 are less clearly related to diffusion, with local maxima observed in many of the datasets. The measurements may primarily reflect the retention of the silver in the graphite, as the SR concentration is on par with the IR and OR. As such, this capsule is not a good candidate for fitting diffusion coefficients, though it may have some utility in calculating the solubility of silver.

Strontium concentration measurements shown in Figure 17 have large gradients at the inner and outer surfaces of the rings, with an unexplainedly large concentration on either side of the gap between the IR and OR. For the measurements at the center of the capsule, the radial concentration profile is inverted, suggesting that a temperature-dependent solubility (activity) model of strontium is warranted. This does not, however, address the steep gradients at the ring edges. The best-fit model for this dataset may be to use the analytical fit described in (Humrickhouse et al. 2016) with boundary conditions set by scaling the simulated concentration at the inner edge of the IR to the final observed concentration at each gap location. Alternately, a 2-D convective-diffusion model may be able to adequately capture the relevant physics if it includes a temperature-dependent activity.

The edges of the rings in the Capsule 3 europium concentration profiles shown in Figure 18 have large concentration gradients, which may yield diffusion information worth consideration. However, the inverted concentration profile in the compact raises questions about solubility or alternate sources. Potential contamination of the R-DLBL samples seems unlikely based on the concentration profiles of the other isotopes.
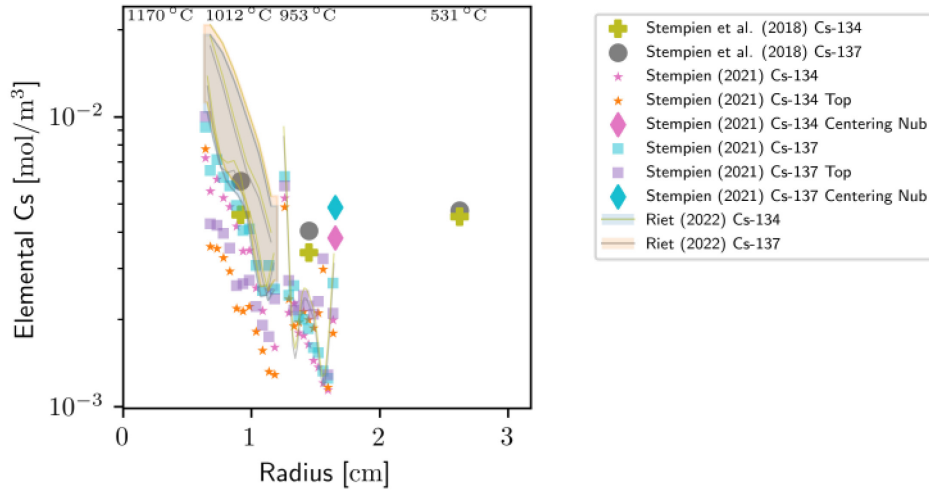

Figure 15. Capsule 3 cesium concentration profiles and overall ring concentrations with tomographic results. Shaded region represents the range between minimum and maximum tomographically reconstructed concentration profiles taken at different axial locations.
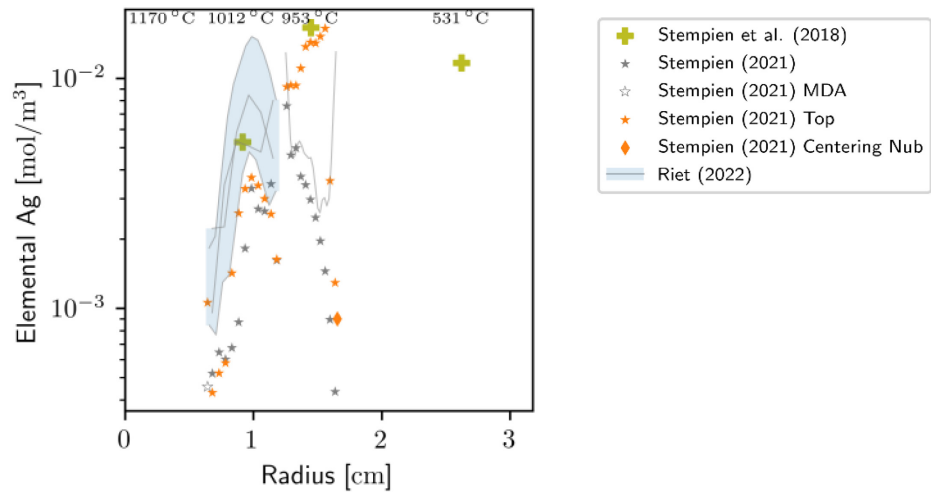
Figure 16. Capsule 3 silver concentration profiles and overall ring concentrations.
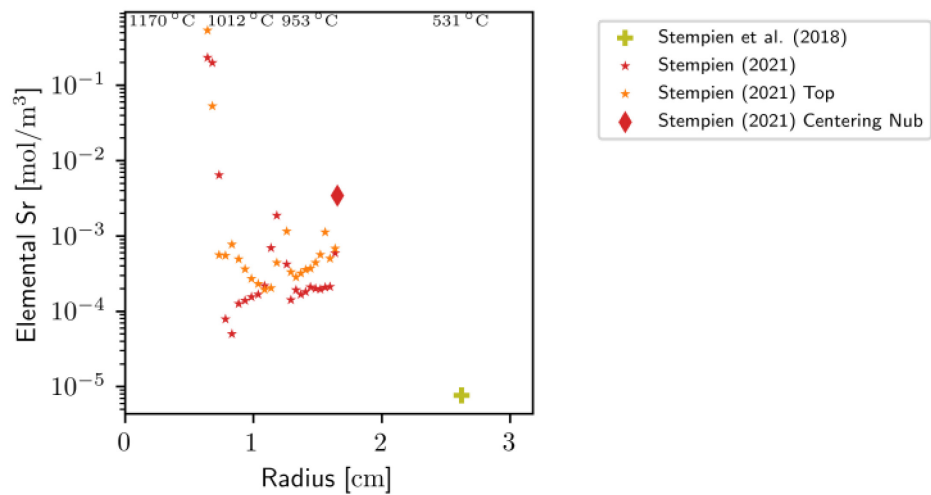

Figure 17. Capsule 3 strontium concentration profiles and overall ring concentrations.
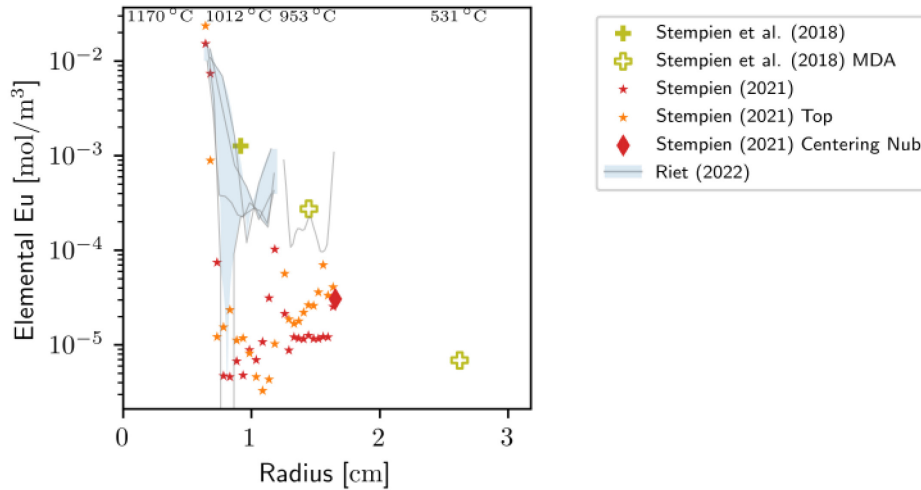
Figure 18. Capsule 3 europium concentration profiles and overall ring concentrations.

3.2.4 Capsule 4

Capsule 4 is an FB with a matrix IR and a PCEA OR and SR. Capsule 4 had compact burnups of 13.98–14.41% FIMA, with compact fast neutron fluences of 4.74–4.92 (10^{25} n/m^2, E > 0.18 MeV) at the end of irradiation (Collin et al. 2018). The time-average peak temperature within the compacts was 1084°C. The TAVA temperatures of the compacts, inner, outer, and SRs were 1008, 820, 708, and 582°C, respectively (Hawkes 2016), and the calculated axial variation in temperature was less than 165°C for the compact, 88°C for the IR and 18°C for the OR. There were no as-irradiated Compact R-DLBL analyses carried out on Capsule 4 compacts; however, Compact 4-3's R-DLBL was taken after a reirradiation in NRAD followed by 1000°C heating in FACS for 300 h (Helmreich et al. 2022) and may be incorporated into future models.

Capsule 4 was the only FB in the AGR-3/4 experiment that was disassembled and analyzed. Capsules 4 and 5 were the only two capsules where the fuel compacts were stuck in the IRs and had to be forced out using a press in the hot cell (Stempien et al. 2016). Both capsules had similar irradiation conditions (e.g., temperature and fluence). Both had rings constructed from the same materials, but one was an FB and one was a standard capsule. Thus, it was decided in 2022 that the Capsule 4 rings should be subjected to destructive physical sampling in an attempt to determine whether evidence of axial gas-gap transport seen in other capsules is also present in an FB capsule with its sealed OR.

Capsule 4 has the most concentration profile information available of all the capsules, and is the only capsule with top, middle, and bottom physical sampling recorded. There is some scatter in measured concentrations, especially in the outside of the OR, but the IR profiles for top, middle, and bottom are all very close together. Capsule 4 is especially useful for fitting because the compact and IR are made from nominally the same material.

Concentration profiles of cesium shown in Figure 19 show a steep concentration gradient across the IR which will likely be useful in fitting. There is less certainty about the utility of the OR, as confounding factors may be contributing to transport. In the OR, for both [134]Cs and ^{137}Cs, there is a higher concentration in the bottom of the ring than the midplane.

The magnitude of silver release was small enough that many measurements were unable to detect [110m]Ag, as demonstrated in Figure 20. Nevertheless, there is a consistent gradient for approximately the first half of the IR in the ring midplane, which may be fit to obtain an estimate of silver diffusivity. A similar strategy as described above whereby an analytical fit with custom-scaled boundary conditions may also help to obtain more information on silver diffusion, though the profile may not be indicative of diffusion in general, so caution should be used.

We observe a strontium concentration profile in Figure 21 similar to that found in Figure 17, with ring concentration profiles that have steep gradients on the ends, and are increasing with radius, which is not typically associated with diffusion, though a temperature-dependent activity may account for this.

Europium concentration profiles observed in Figure 22 also follow the trends noted in reference to strontium, with the exception that there is no appreciable decrease in concentration across the gas gap between the IR and OR, indicating more efficient gas-phase transport. This may be expected based on the comparatively lower vapor pressure of europium than strontium (Spedding, Hanak, and Daane 1958; De Maria and Piacente 1974). Perhaps most interesting is that the large concentration gradient observed in the compact is not replicated in the rings, as if there were two transport mechanisms at work—a low-resistance pathway for trace amounts and a higher-resistance pathway for bulk transport. It is likely that an estimate for bulk diffusivity can be estimated, but analyzing the (fast) transport of trace quantities of cesium (such as those in the OR) would likely require more experiments.
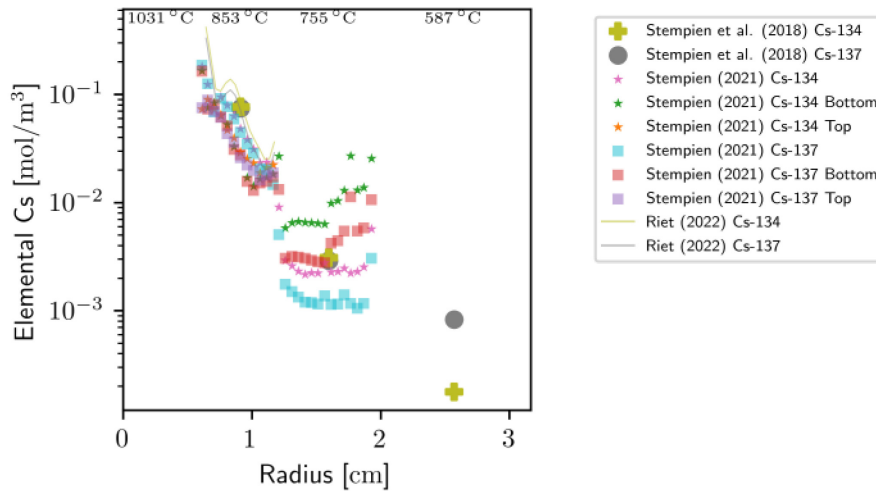

Figure 19. Capsule 4 cesium concentration profiles and overall ring concentrations.
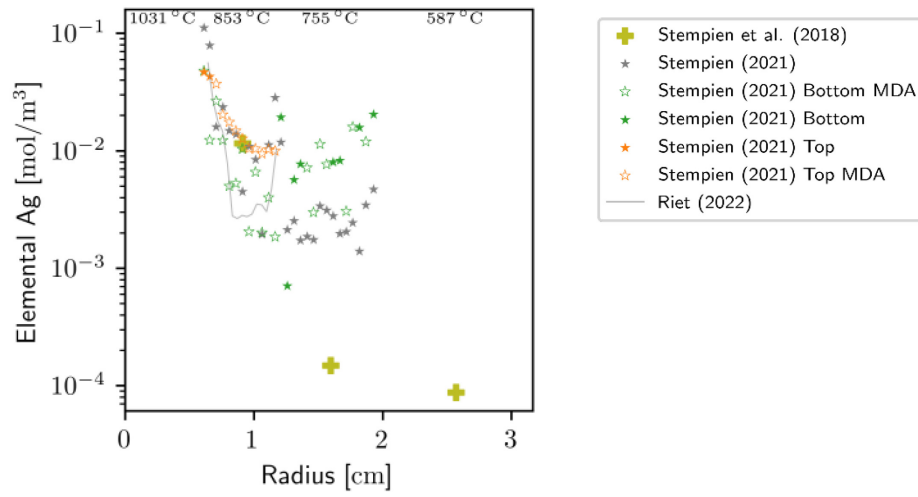
Figure 20. Capsule 4 silver concentration profiles and overall ring concentrations.
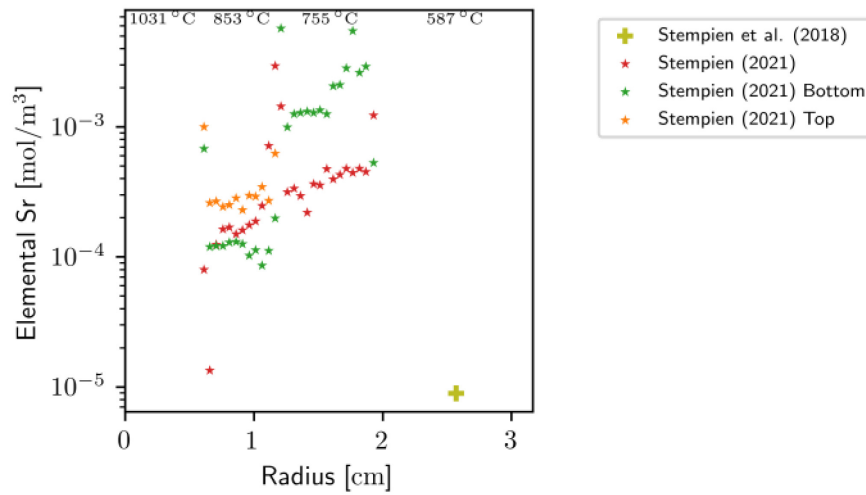

Figure 21. Capsule 4 Strontium concentration profiles and overall ring concentrations.
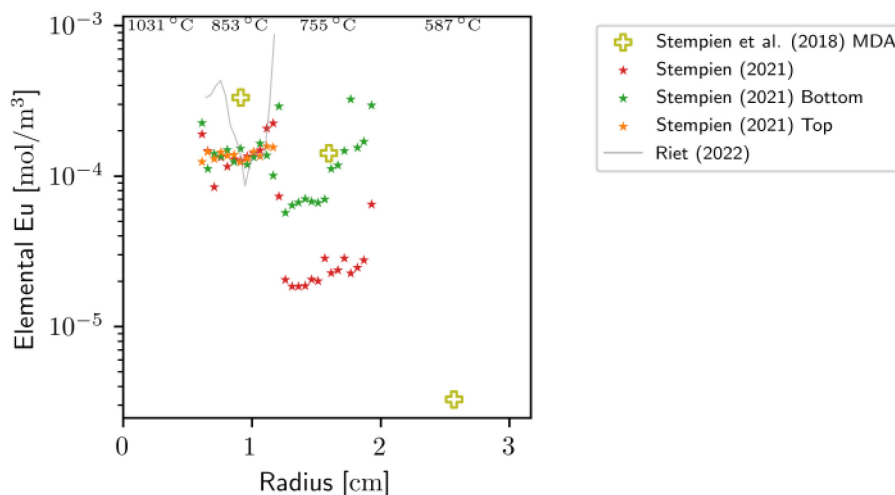
Figure 22. Capsule 4 europium concentration profiles and overall ring concentrations.

3.2.5 Capsule 5

Capsule 5 is a standard capsule with a matrix IR and PCEA outer and SRs. The fuel in Capsule 5 had compact burnups of 14.74–14.98% FIMA, with compact fast neutron fluences of 5.14–5.23 (10^{25} n/m², E > 0.18 MeV) at the end of irradiation (Collin et al. 2018). The time-average peak temperature within the compacts was 1102°C. The TAVA temperatures of the compacts, inner, outer, and SRs were 1015, 800, 677, and 546°C, respectively (Hawkes 2016), and the calculated axial variation in temperature was less than 219°C for the compacts, 96°C for the IR, and 27°C for the OR. As stated earlier, Capsules 4 and 5 were the only two capsules where the fuel compacts were stuck in the IRs and had to be forced out using a press in the hot cell (Stempien et al. 2016). R-DLBL measurements of Compact 5-3 and 5-4 will be the subject of a forthcoming INL report, though the relevant data have been reproduced as triangles in Figure 23–Figure 27.

Capsule 5 was only destructively measured at the center of the ring. Within each ring, the measurements follow mostly smooth decreasing gradients radially outward, to the extent that data is available, and appear to be consistent with a diffusive profile. The IR of Capsule 5 was similar to Capsule 4, and the close average temperatures of the compacts and rings in Capsules 4 and 5 provide an opportunity for error estimation.

As shown in Figure 23, the cesium concentration profile is almost monotonically decreasing as a function of radius through to the OR, which should allow at least fits of diffusivity for each individual ring and the compact. The elevated concentration at the outside of the compact does not match this trend. The relatively flat low concentration in the outer and SRs may indicate a low-energy trace transport pathway.

Silver concentrations in Capsule 5 are small enough that many measurements fell below the MDA. The overall OR concentrations shown in Figure 24 suggest that there is likely more activity on the ring top and/or bottom edges than in the center, though this is not conclusively demonstrated in azimuthal profile scanning using the PGS (Riet 2022). The IR tomographic scan concentration profile is prone to overestimate activity when concentrations are near the MDA, and is not likely to be reliable as an estimator (Riet 2022).

Strontium concentrations shown in Figure 25 follow a diffusive profile within the compact, though concentrations are low enough in the IR (save for the innermost edge) that few samples had quantifiable ^{90}Sr inventory. OR concentrations seem to be larger than the IR concentrations, with increasing concentrations as the radius increases over the outer 2/3 of the ring. While likely not useful in estimating strontium transport parameters directly, the OR of Capsule 5 may serve as a useful check on any extracted properties.

Europium concentration in Capsule 5 compact and innermost segments of the IR, shown in Figure 26, may be fit to the same Fickian diffusion model if the appropriate sorptivity ratio between the compact and IR is assumed. The OR concentration profile does not bear a clear relationship to radial transport.
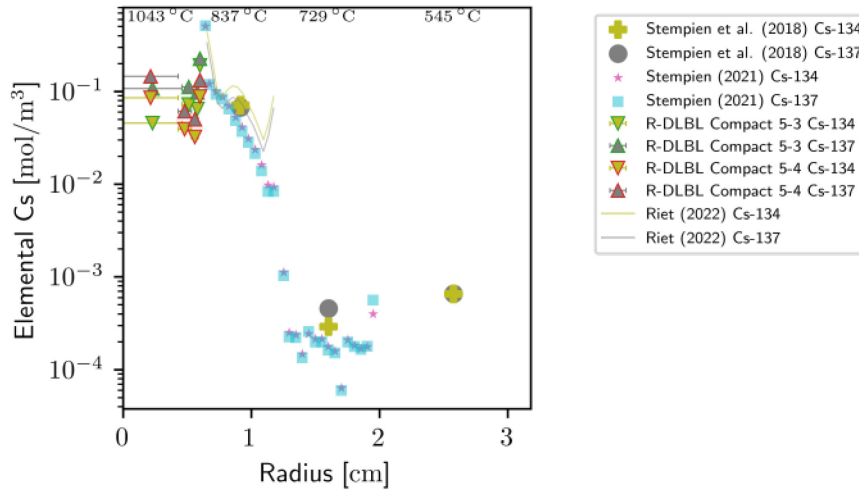

Figure 23. Capsule 5 cesium concentration profiles and overall ring concentrations.
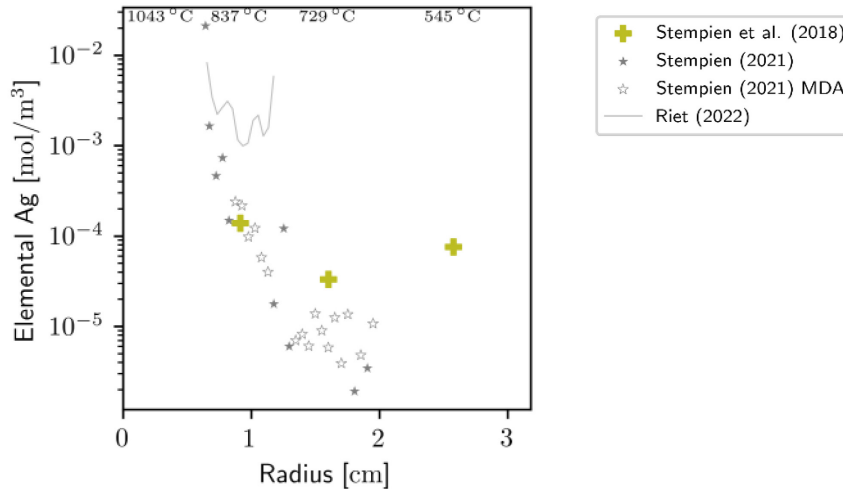

Figure 24. Capsule 5 silver concentration profiles and overall ring concentrations.
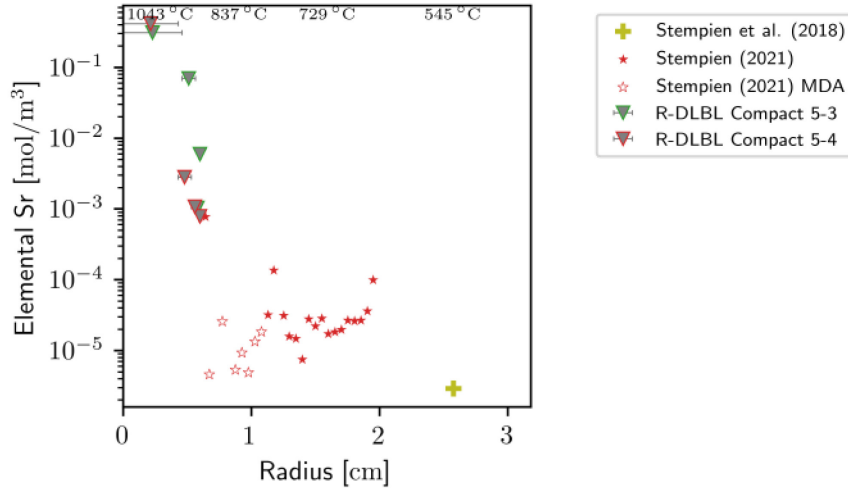
Figure 25. Capsule 5 Strontium concentration profiles and overall ring concentrations.
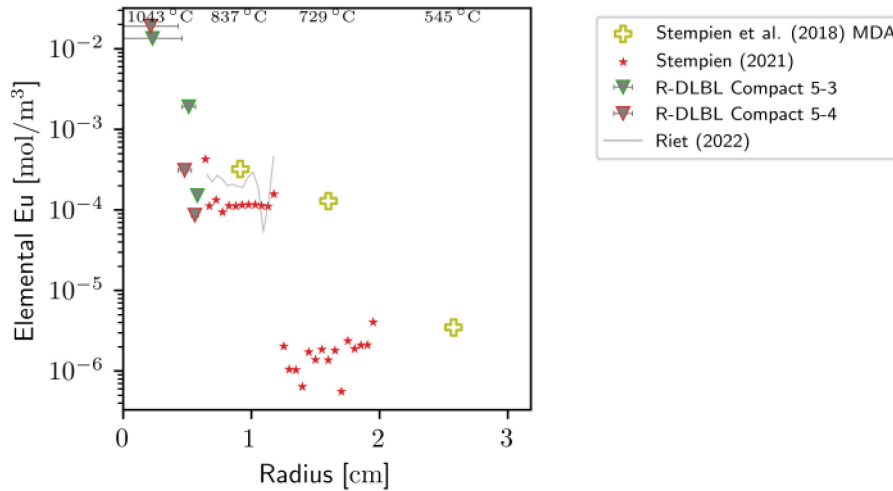

Figure 26. Capsule 5 europium concentration profiles and overall ring concentrations.

3.2.6 Capsule 6

Capsule 6 was an FB capsule with a matrix IR and PCEA outer and SRs. It was retained intact; therefore, information on the fission product profiles and inventories of the IR and OR are not available. Capsule 6 had compact burnups of 15.21–15.24% FIMA and compact fast neutron fluences of 5.30–5.32 (10^{25} n/m², E > 0.18 MeV) at the end of irradiation (Collin et al. 2018). The time-average peak temperature within the compacts was 1133°C. The TAVA temperature of the compacts, inner, outer, and SRs were 1051, 843, 707, and 603°C, respectively (Hawkes 2016), and the calculated axial variation in temperature was less than 222°C for the compacts, 116°C for the IR, and 27°C for the OR.

As Capsule 6 is an FB capsule, the only recorded inventories are in the SR. Like Capsule 2, it will be used for verification, not fitting of transport parameters. Figure 27–30 show the concentrations derived from the measured SR inventories and MDAs.
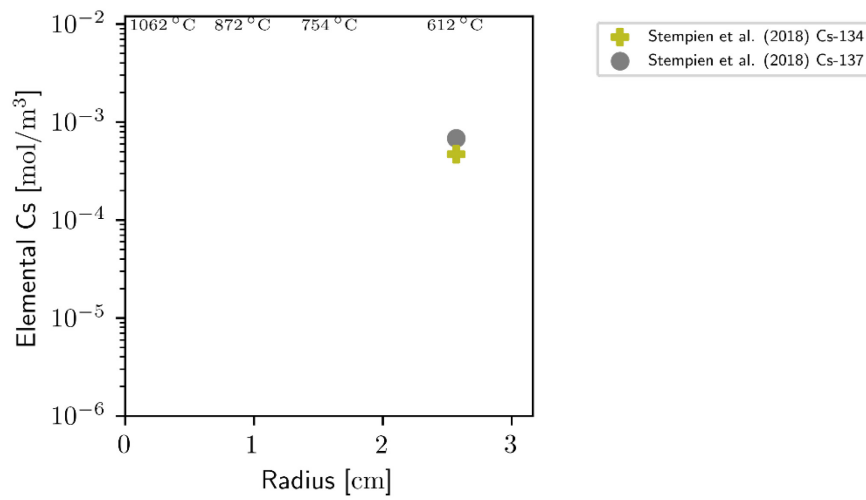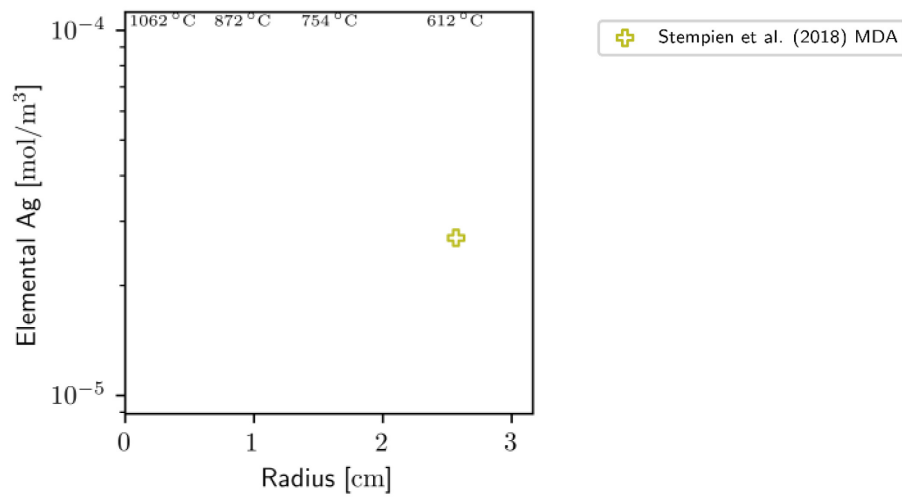
Figure 27. Capsule 6 cesium SR inventory.

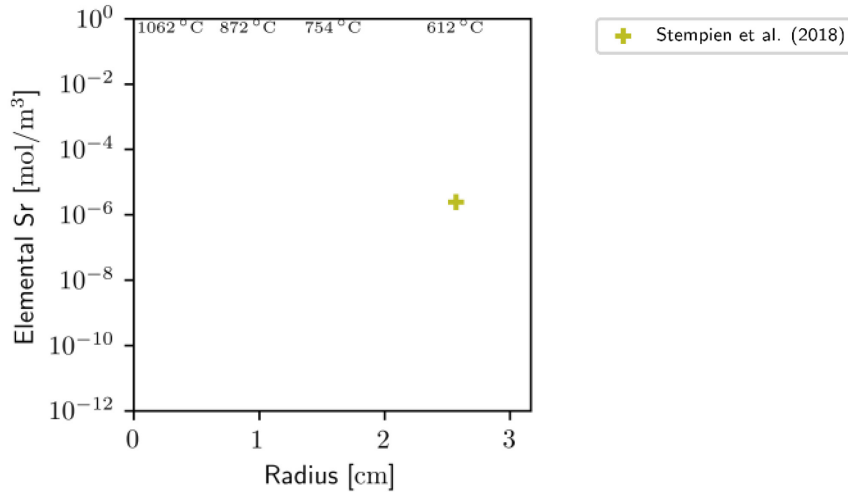Figure 28. Capsule 6 silver SR MDA concentration.
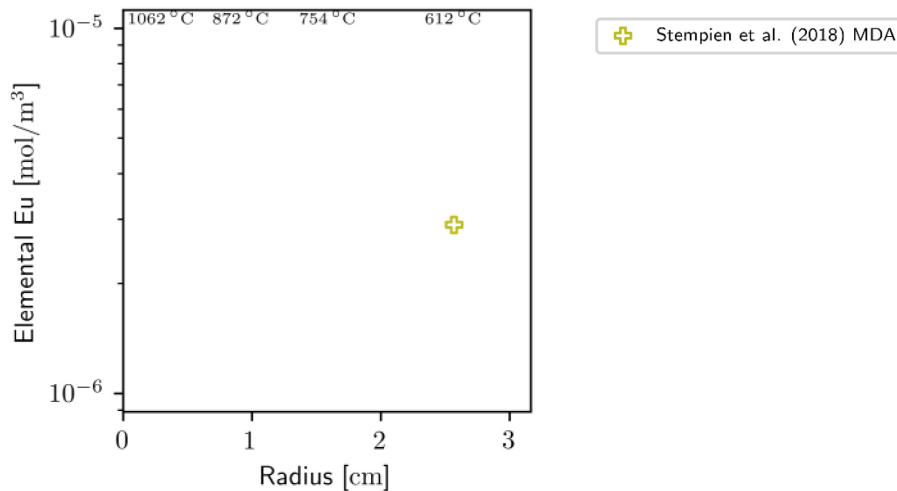
Figure 29. Capsule 6 strontium SR inventory.

Figure 30. Capsule 6 europium SR MDA concentration.

3.2.7 Capsule 7

Capsule 7 was a standard capsule with a matrix IR and OR and PCEA SRs. Capsule 7 compacts had burnups of 14.90–15.02% FIMA, with compact fast fluences of 5.24–5.29 (10^{25} n/m^2, E > 0.18 MeV) at the end of irradiation (Collin et al. 2018). The time-average peak temperature within the compacts was 1418°C. The TAVA irradiation temperature of the compacts, inner, outer, and SRs were 1345, 1151, 1025, and 617°C, respectively (Hawkes 2016), and the calculated axial variation in temperature was less than 192°C for the compacts, 90°C for the IR and 23°C for the OR. Compact 7-3 R-DLBL will be the subject of a forthcoming INL report, and Compact 7-4 R-DLBL has been described previously (Helmreich et al. 2021).

The outermost layer of Compact 7-3's R-DLBL data has been adjusted to account for a single particle failure in the outer layer during the deconsolidation process (not during irradiation) by subtracting the inventory of a single particle from the total.

Capsule 7 was the hottest capsule under irradiation and had multiple compact concentration profile measurements through radial deconsolidation, as well as destructive sampling and tomography at multiple locations. Much of the data measured had good counting statistics with activities much higher than the MDA and there is a clear correlation of isotope activity with respect to radial position, making this a good candidate for deriving high-temperature diffusion characteristics. In contrast to Capsule 3, concentrations found in the centering nub are much lower than the nearby bulk, with the exception of strontium. Comparison of Compact 7-3 and 7-4 outer segment concentrations shows a large discrepancy (>10×) in cesium concentrations. This effect may be due to the correction of the particle failure, but the discrepancy was not observed for the other measured isotopes.

The cesium concentration profile for Compact 7-4 (shown in Figure 31) has an unusual characteristic in that it increases at the outer edge of the compact. This effect is not observed in its neighbor, Compact 7-3. Aside from this, the radial concentration profiles follow the generally expected trend for radial diffusion and should allow for model fitting.

Figure 32 shows the concentration profiles observed for silver. The IR may be useful in generating a diffusion profile, but the OR indicates behavior that is more complex than pure radial diffusion. Capsule 7 is a candidate for 2-dimensional convection-diffusion modeling to see if the concentration profiles recorded can be explained by that model.

Strontium concentrations shown in Figure 33 seem consistent with those found in other capsules, with concentrations that increase in the radial direction for the majority of the IR and OR, and a steep decreasing concentration gradient at the inner surface of the ring. Compacts 7-3 and 7-4 are quite similar with regard to strontium inventory, in contrast to the observations with regard to cesium.

Europium, depicted in Figure 34, has a compact concentration profile not unlike that observed in Capsule 3, with similarities to recorded strontium concentrations, such as the radially increasing concentration profile over the bulk of the IR and OR, and in this case, the compact. While effective diffusion coefficients may be able to fit to specific regions (such as the steep concentration gradient at the inner edge of the IR and OR), model parameters resulting from such a fit are still subject to uncertainty with respect to the radially increasing concentrations, without finding a suitable model with a temperature-dependent activity of transport.
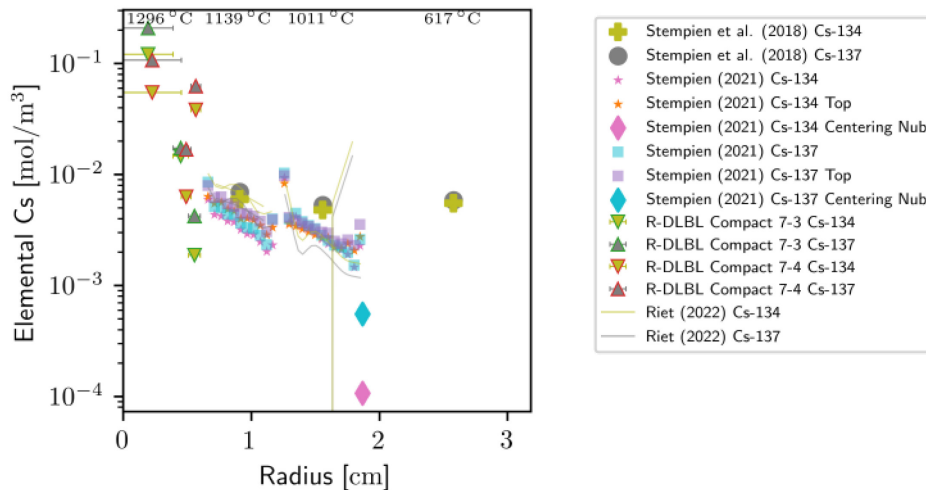

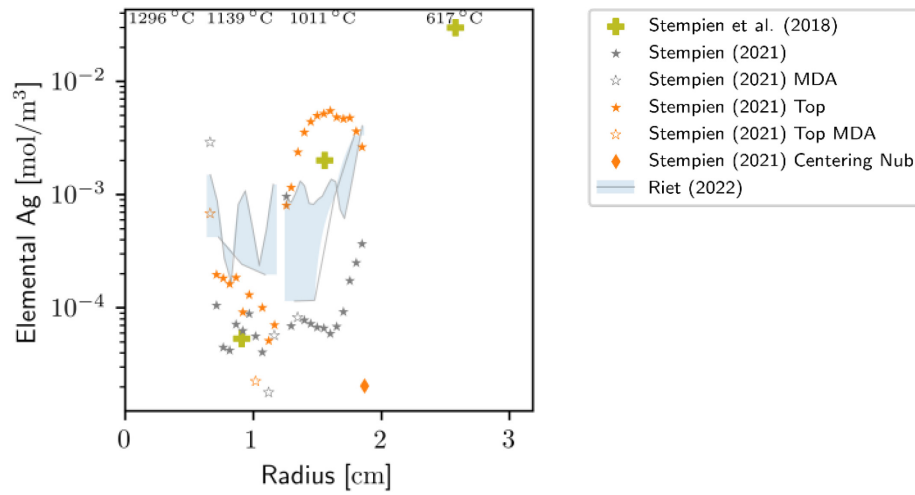Figure 31. Capsule 7 cesium concentration profiles and overall ring concentrations.

Figure 32. Capsule 7 silver concentration profiles and overall ring concentrations.
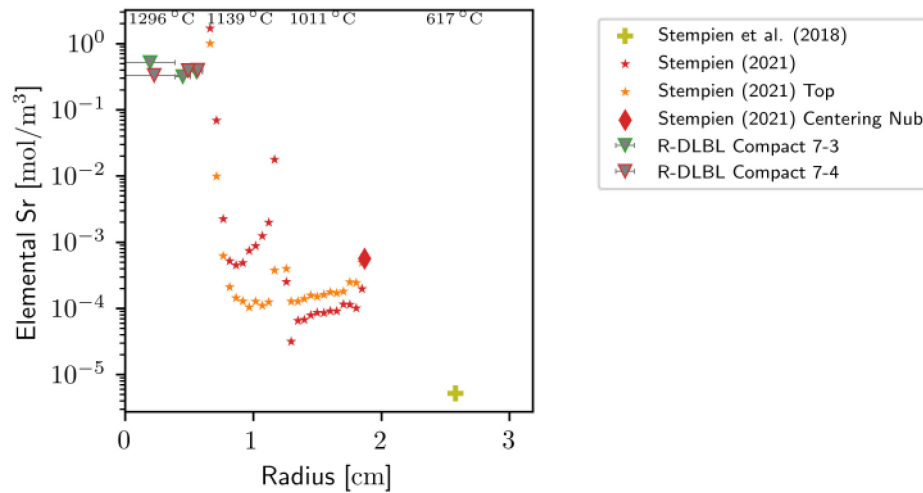

Figure 33. Capsule 7 strontium concentration profiles and overall ring concentrations.
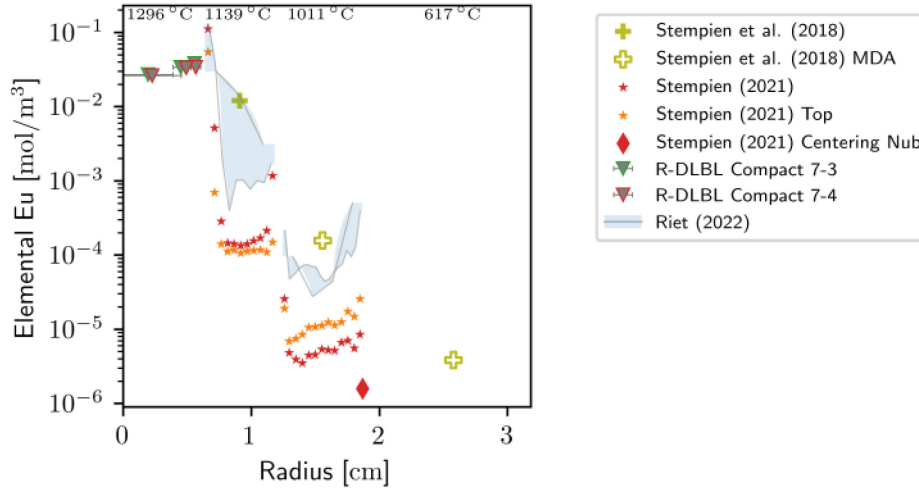
Figure 34. Capsule 7 europium concentration profiles and overall ring concentrations.

3.2.8 Capsule 8

Capsule 8 is a standard capsule containing the only IG-110 IR used in AGR-3/4, one of two IG-110 ORs (the other was in Capsule 9), and a SR made of PCEA. Capsule 8 compacts had burnups of 14.43–14.58% FIMA, with fast neutron fluences of 5.02–5.13 (10^{25} n/m^2, E > 0.18 MeV) at the end of irradiation (Collin et al. 2018). The time-average peak temperature within the compacts was 1257°C. The TAVA irradiation temperature of the compacts, inner, outer, and SRs were 1190, 1021, 917, and 582°C, respectively (Hawkes 2016), and the calculated axial variation in temperature was less than 141°C for the compacts, 66°C for the IR and 37°C for the OR. Capsule 8 also had multiple compact R-DLBLs. Compact 8-4 was the subject of an ORNL report (Helmreich et al. 2021), while Compact 8-3 R-DLBL is the subject of a forthcoming INL report. Compact 8-2 R-DLBL is not directly comparable to 8-3 and 8-4 as it was heated at 1400°C in the FACS furnace prior to R-DLBL. The multiple compact measurements along with the destructive sampling in multiple locations on the rings should allow for a more robust model fit.

Cesium concentrations shown in Figure 35 are the most complex profiles, with what appears to be considerable scatter in the compact concentration profiles and OR concentrations greater than those of their IR counterparts.

Silver concentration profiles obtained are shown in Figure 36, which demonstrate a clear relationship between radial position and concentration. This relationship is shared between measurements at the axial midplane and bottom of the compact and is also consistent with tomographic reconstructions. Modeling the specific transport processes that gave rise to the observed concentration profile may prove a challenge. Given that the silver transport at the relevant temperatures is predicted to be very fast in Capsule 8, the observed behavior may be a result of silver solubility and trapping.

Strontium concentrations shown in Figure 37 follow a largely continuous concentration profile that seems very consistent between the compacts and the rings, making Capsule 8 an ideal candidate to extract transport parameters for strontium, though we do observe a small increase in concentration as the OR radius increases.

Europium concentrations in Figure 38 are also consistent between compacts and the IR, though there is not as much agreement between the destructive analyses at the different locations as there is for strontium. Given the large concentration gradient followed by a small concentration gradient for the bottom destructive analyses in the IR, a fast-slow dual-path diffusion model is likely to fit the data well.
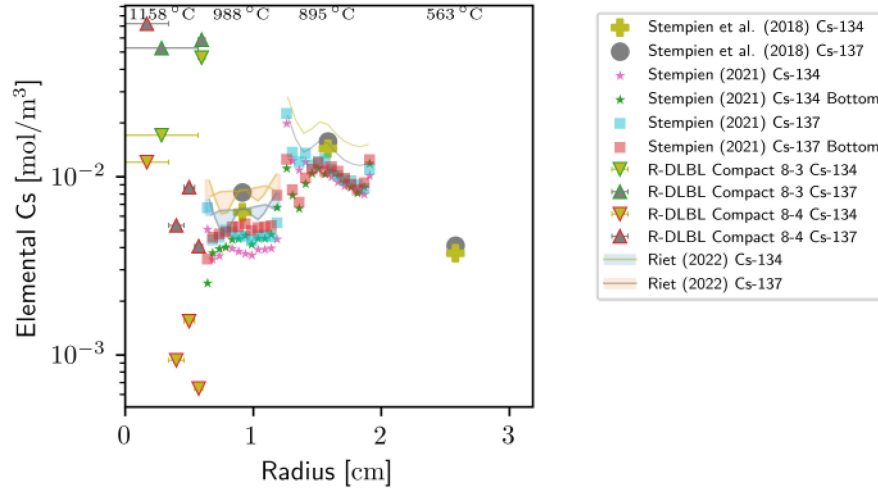
Figure 35. Capsule 8 cesium concentration profiles and overall ring concentrations.
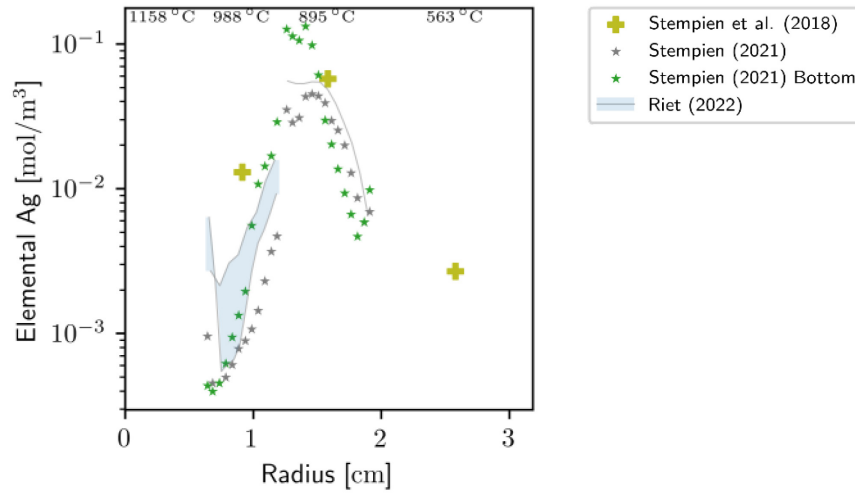

Figure 36. Capsule 8 silver concentration profiles and overall ring concentrations.
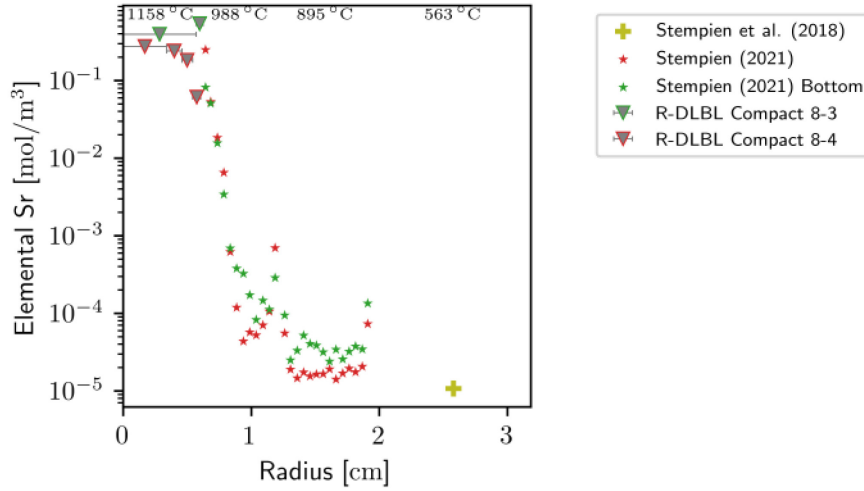
Figure 37. Capsule 8 strontium concentration profiles and overall ring concentrations.
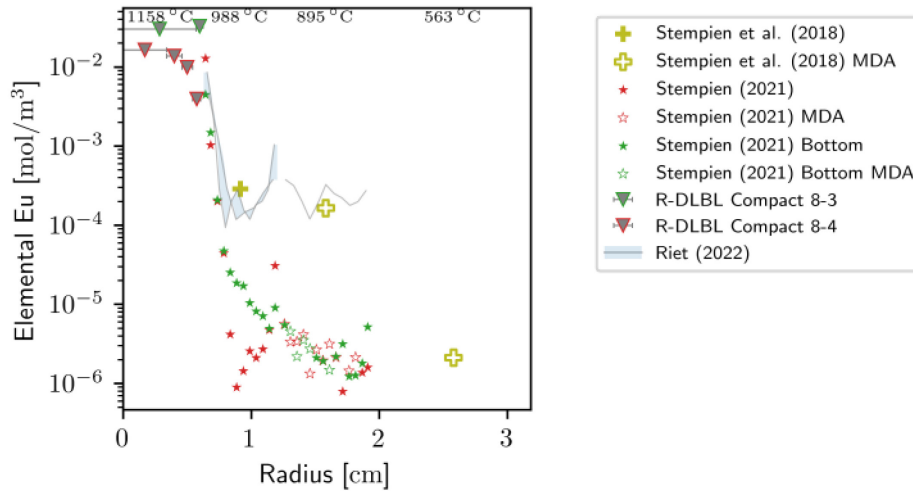

Figure 38. Capsule 8 europium concentration profiles and overall ring concentrations.

3.2.9   Capsule 9

Capsule 9 is an FB capsule that was retained intact. Its IR was made of matrix material, its OR was made of IG-110, and its SR was PCEA. Capsule 9 compacts had burnups of 13.40–13.87% FIMA, and fast neutron fluences of 4.53–4.76 (10^{25} n/m^2, E > 0.18 MeV) at the end of irradiation (Collin et al. 2018). The time-average peak temperature within the compacts was 1083°C. The TAVA irradiation temperature of the compacts, IR, OR and SR were 1008, 822, 698, and 608°C, respectively (Hawkes 2016), and the calculated axial variation in temperature was less than 168°C for the compacts, 106°C for the IR and 28°C for the OR. Because the Capsule 9 FB was retained intact, data on the IR and ORs are unavailable. Capsule 9 SR inventories will be used for verification of the models fit to other capsules, see Figure 39–Figure 42.
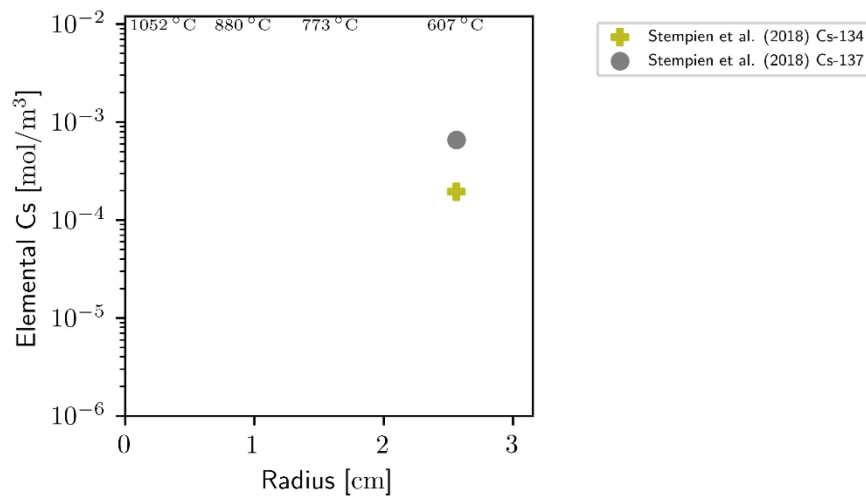
Figure 39. Capsule 9 cesium SR inventory.
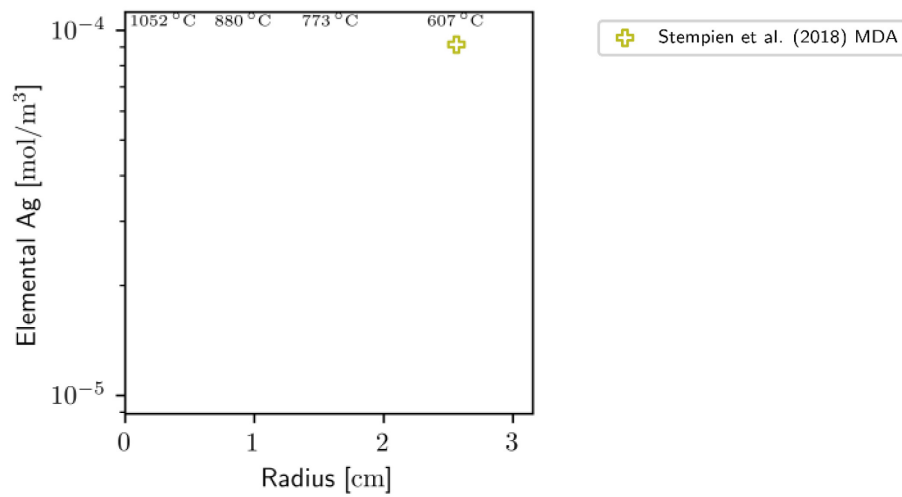
Figure 40. Capsule 9 silver SR MDA concentration.
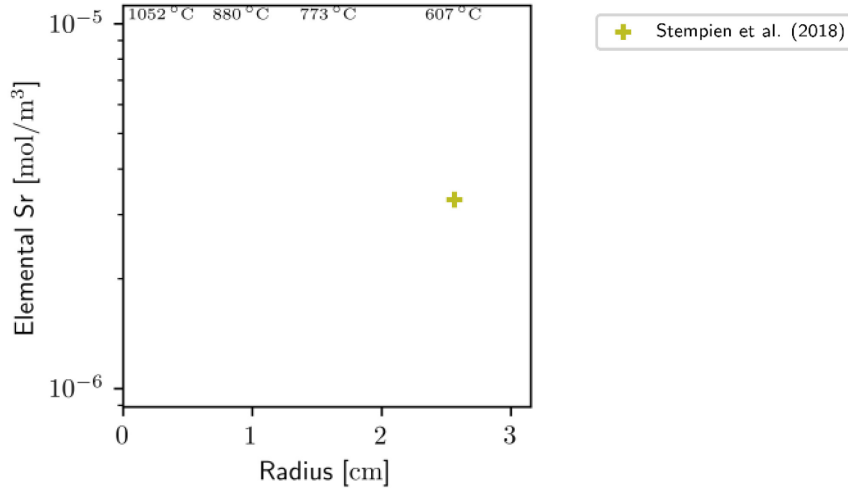
Figure 41. Capsule 9 strontium SR MDA concentration.
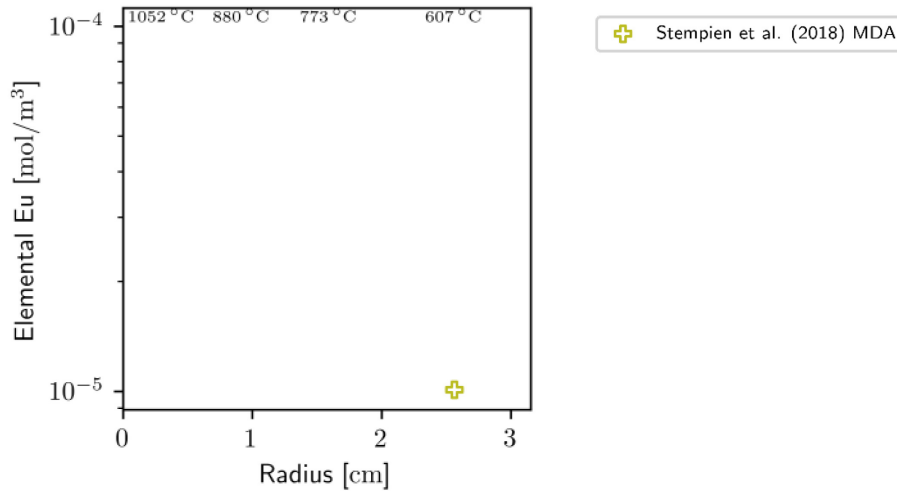
Figure 42. Capsule 9 europium SR MDA concentration.

3.2.10   Capsule 10

Capsule 10 is a standard capsule with all rings made from PCEA, similar to Capsule 3. Capsule 10 compacts have burnup of 11.43–12.08% FIMA and compact fast neutron fluences of 3.75–4.12 (10^{25} n/m^2, E > 0.18 MeV) at the end of irradiation (Collin et al. 2018). The time-average peak temperature within the compacts was 1249°C. The TAVA irradiation temperature of the compacts, inner, outer, and SRs were 1191, 1038, 971, and 646°C respectively (Hawkes 2016), and the calculated axial variation in temperature was less than 129°C for the compacts, 34°C for the IR and 12°C for the OR. R-DLBL was carried out on Compacts 10-1, 10-2 and 10-4, though these capsules were the subject of heating tests at 1400°C and 1200°C respectively before deconsolidation (Hunn et al. 2020), which will need to be incorporated into the models before valid comparisons can be made.

Concentration profiles for cesium in Capsule 10 are generally radially decreasing, and ^{134}Cs and ^{137}Cs generally show similar concentrations as a function of radius, even when taken between the midplane and bottom of the ring, though the ^{134}Cs concentrations in the bottom of the OR are elevated with respect to the other measurements. A one-dimensional radial profile may be able to fit the data well, though it would constrain the sorptivity ratio across the gaps between rings. See Figure 43.

Figure 44 shows silver concentrations in Capsule 10 exhibit similar peaks to those in 3, 7, and 8—though not 4 or 5. The final profiles do not decrease radially outward from the location of the isotopic source. This would seem to be more consistently modeled as an equilibrium concentration profile, at least for the IR measurements, where recorded concentrations reflect solubility and mobility (trapping) more than diffusive transport.

Strontium concentrations in Capsule 10, shown in Figure 45, exhibit characteristics similar to those in all of the capsules for which there is data; a steep concentration gradient on the inner edge of each ring, followed by a radially increasing concentration through the bulk of the ring. There is a small concentration gradient in the data from radial deconsolidation of the compacts, which may be used to calculate transport, in addition to the solubility model described elsewhere.

Europium concentration profiles and overall ring concentrations for Capsule 10 are shown in Figure 46, and exhibit a relatively shallow concentration gradient in the compact, followed by a large concentration gradient in the innermost section of the IR, before moving to a radially increasing concentration for the bulk of the IR and OR. A solubility/mobility model may prove necessary for modelling the rings, though an estimate of the diffusivity in the compact may be straightforward to obtain.

Figure 43. Capsule 10 cesium concentration profiles and overall ring concentrations.
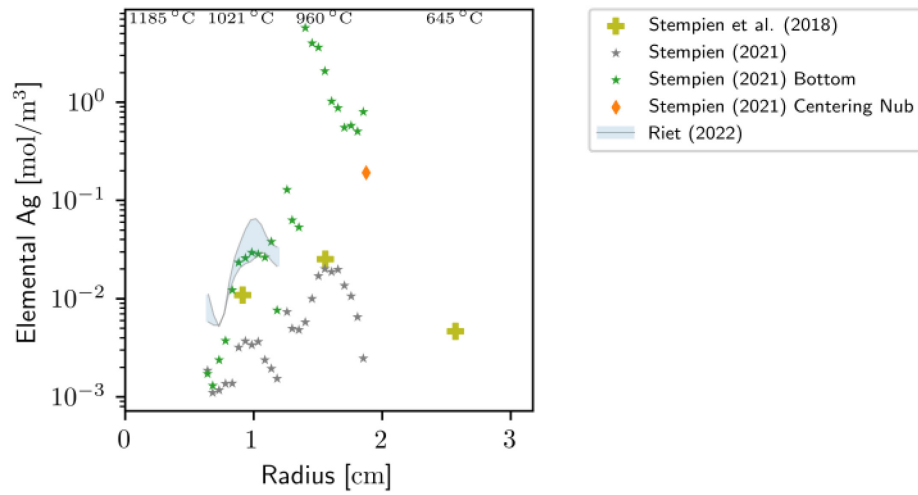
Figure 44. Capsule 10 silver concentration profiles and overall ring concentrations.

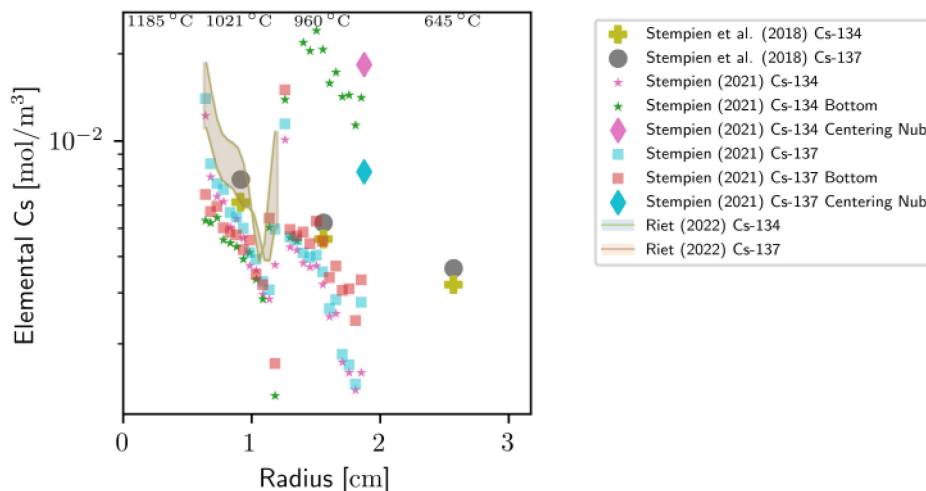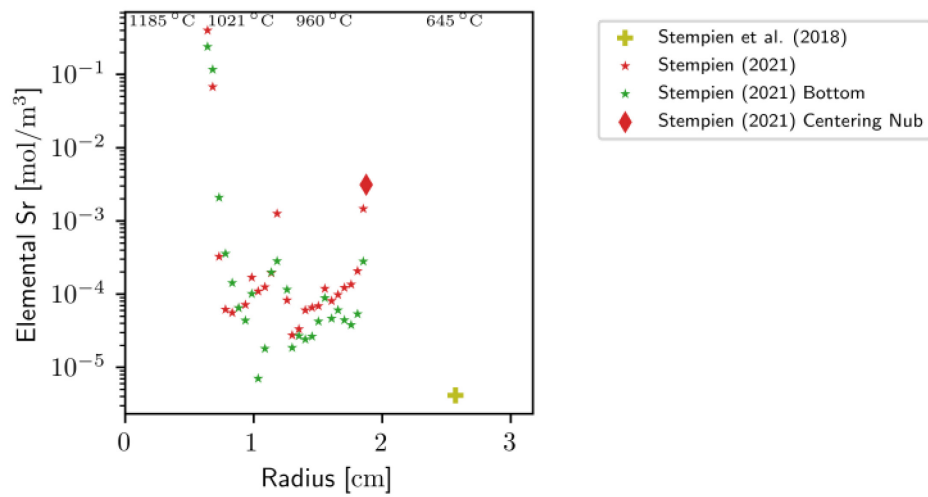Figure 45. Capsule 10 strontium concentration profiles and overall ring concentrations.
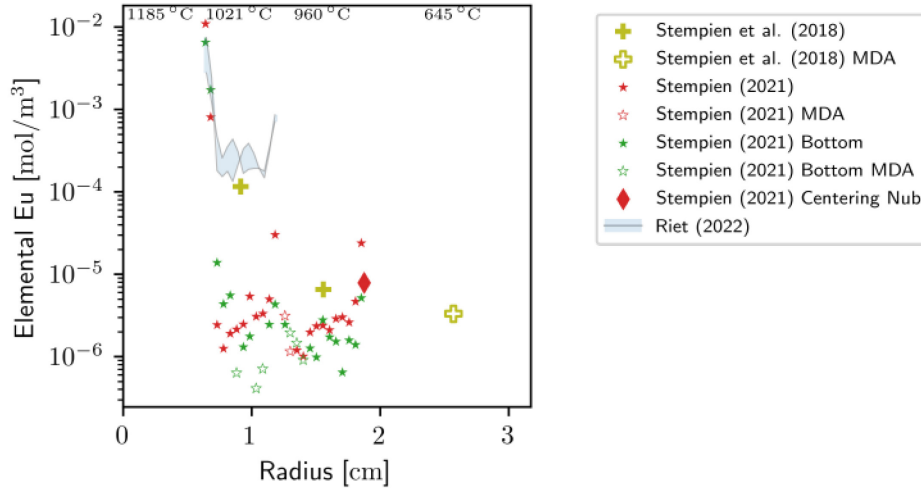
Figure 46. Capsule 10 europium concentration profiles and overall ring concentrations.

3.2.11 Capsule 11

Capsule 11 is an FB with a matrix IR and PCEA outer and SRs. It was retained intact; therefore, the fission product inventories of the IR and ORs have not been measured. Capsule 11 had compact burnups of 8.42–9.64% FIMA and compact fast neutron fluences of 2.61–3.11 (10^{25} n/m^2, E > 0.18 MeV) at the end of irradiation (Collin et al. 2018). The time-average peak temperature within the compacts was 1280°C. The TAVA irradiation temperature of the compacts, inner, outer and SRs were 1226, 1124, 966, and 737°C, respectively (Hawkes 2016), and the calculated axial variation in temperature was less than 125°C for the compacts, 77°C for the IR, and 16°C for the OR.

As Capsule 11 does not have radial profile information, it will be used along with Capsules 2, 6, and 9 to verify the results of modeling efforts on the other rings.

Figure 47. Capsule 11 cesium SR concentrations.

Figure 48. Capsule 11 silver SR concentration.

Figure 49. Capsule 11 strontium SR concentration.

Figure 50. Capsule 11 europium SR MDA.

3.2.12 Capsule 12

Capsule 12 is a standard capsule composed of a matrix IR and PCEA outer and SRs. Capsule 12 had compact burnups of 4.85–5.87% FIMA and compact fast neutron fluences of 1.19–1.80 (10^{25} n/m^2, E > 0.18 MeV) at the end of irradiation (Collin et al. 2018). The time-average pe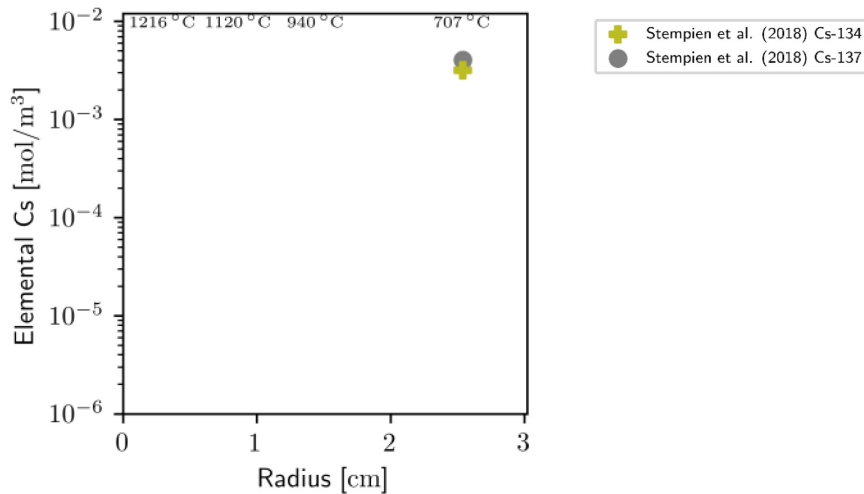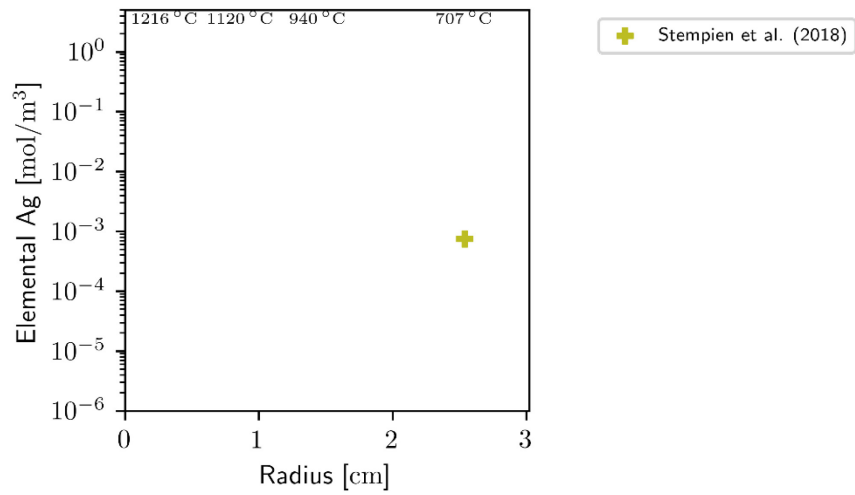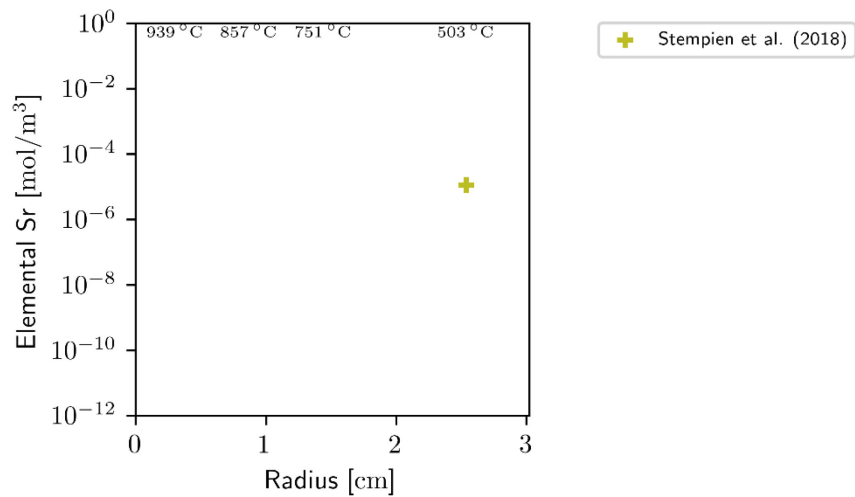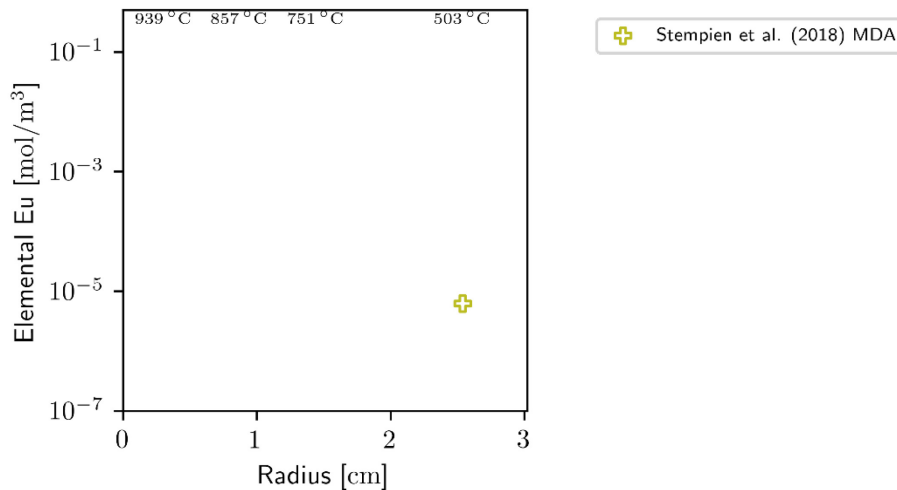ak temperature within the compacts was 888℃. The TAVA temperature of the compacts, inner, outer, and SRs were 854, 782, 741, and 505℃ respectively (Hawkes 2016), and the calculated axial variation in temperature was less than 79℃ for the compacts, 36℃ for the IR and 11℃ for the OR.

Note that a thin outer portion of Compact 12-3 accounts for one of the R-DLBL data points. The second R-DLBL data point represents the relatively large center region of the compact that includes the fission product inventory in the compact matrix, driver particles, and the DTF kernels.

Cesium concentration profiles from Capsule 12 are shown in Figure 51. Though there are limited data from the compact deconsolidations, the destructive analyses provide consistent data, and may allow for a temperature-dependent fit of diffusivity between the compact and IR. The OR concentration profile is not likely to be well described by a one-dimensional model.

Silver concentration profiles are not shown in Figure 52, as there was no statistically significant activity detected in Capsule 12, likely due to the colder temperatures limiting transport and the low burnup in Capsule 12 that would result in relatively low total ^{110m}Ag inventory in the fuel. Only MDAs for all attempted measurements are shown in Figure 52. As briefly discussed by Stempien (2021) in reference to beta-emitter activity interference, the MDAs form a shape that looks like a concentration profile because the background activity of the capsule decreases radially outward, so there is less interference and a lower noise floor as distance from the radial centerline increases.

Strontium concentration profiles are shown in Figure 53, which exhibits a steep concentration profile at the edge of the rings, and generally increasing concentrations moving radially outward for the bulk of the rings. The outer edges have much higher activity than the inner edges, a feature that will be difficult to capture and may not be possible with a one-dimensional model.

Europium concentrations in Figure 54 appear to show diffusive transport through the compact, with a flat profile in the IR, followed by a sharp concentration gradient at the inner edge of the OR, and then radially increasing concentrations for the bulk of the OR for both bottom and centerline destructive measurements. Applying the temperature-based activity model will likely change the apparent concentration gradient in the IR.
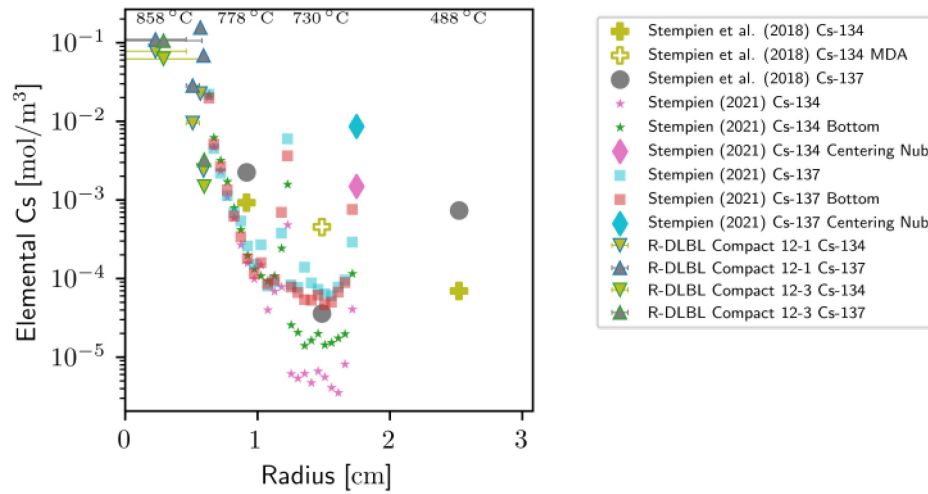
Figure 51. Capsule 12 cesium concentration profiles and overall ring concentrations.
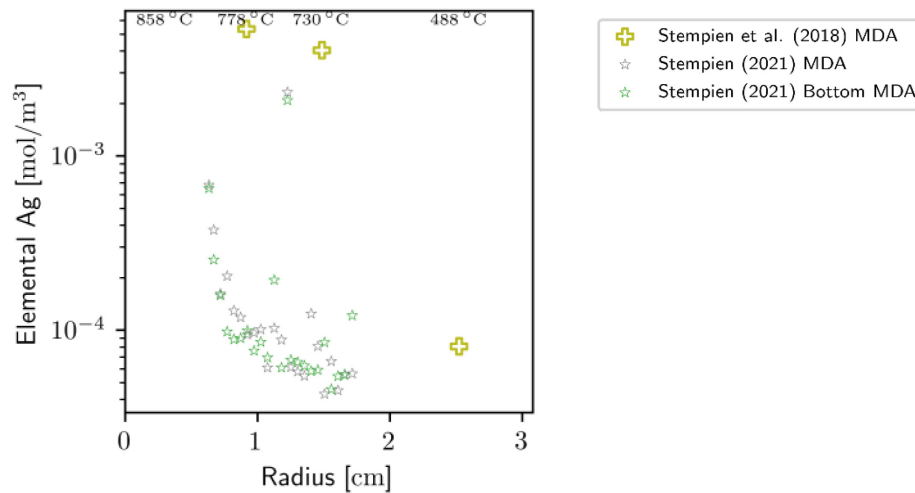
Figure 52. Capsule 12 silver MDA concentrations and overall ring concentration MDAs. No silver was detected outside the fuel compacts in Capsule 12.
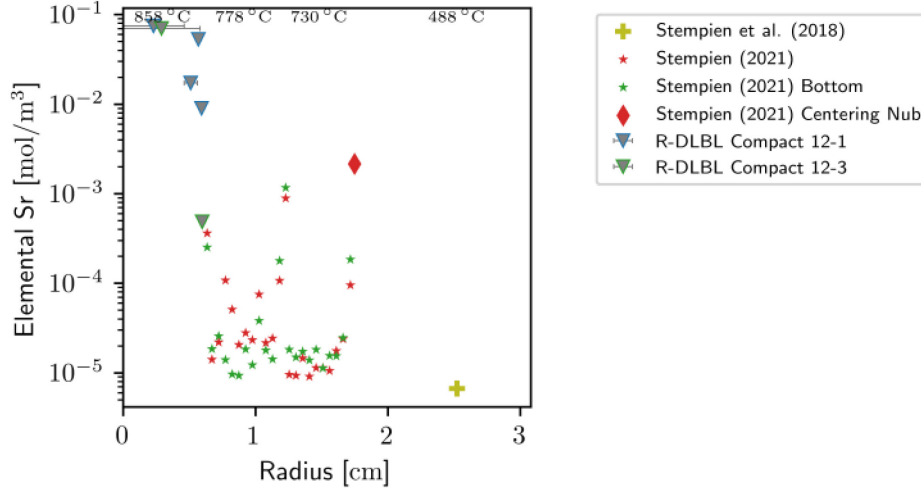
Figure 53. Capsule 12 strontium concentration profiles and overall ring concentrations.
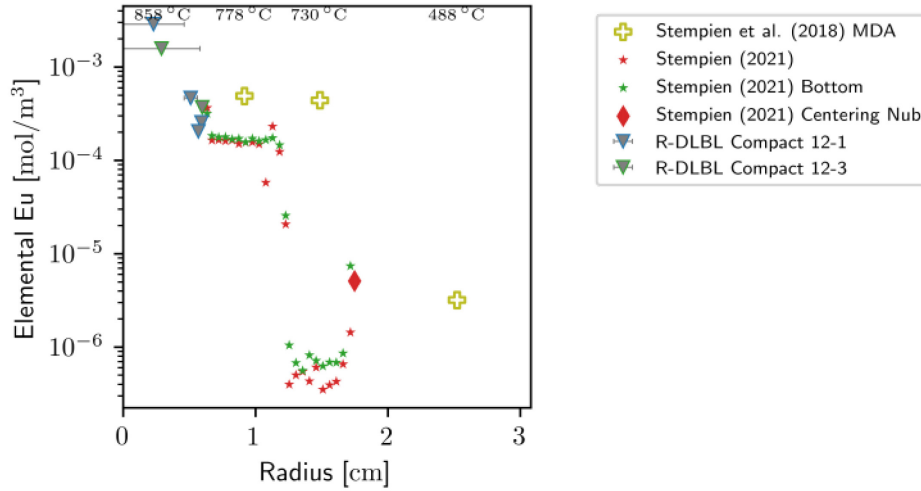
Figure 54. Capsule 12 europium concentration profiles and overall ring concentrations.

4. DISCUSSION AND FUTURE WORK

One-dimensional time-averaged constant temperature transport models were compared to the available experimental data (without compact R-DLBLs) (Riet and Stempien 2022). In many cases, the legacy parameters can be reasonably used to predict the observed transport. In cases where a simple radially diffusive model captures the physical processes well (based on reasonably close comparisons to the measured data including new R-DLBL analyses), the desire is to extract new diffusivities by fitting the model to the data. In cases where the model does not seem to capture some important physics, it may not be possible to extract such diffusivities unless the model can be improved.

Several model types will be used to fit the data for the separate capsules. The simplest model available is a time-dependent analytical fit of diffusion in an individual ring with specified boundary conditions. Moving up in complexity, a finite-element Fickian diffusion model of the capsule with source terms calculated by JMOCUP (Sterbentz 2015) and fuel compact release rates calculated by PARFUME (Skerjanc 2016), and temperature profiles from the as-run report (Hawkes 2016) implemented in the BISON fuel-performance code in the MOOSE simulation framework (Lindsay et al. 2022; Williamson et al. 2021) can be used to fit to either the compacts and individual rings, or the whole of the available data for a capsule. Adding more complexity, a temperature-dependent trapping model may be necessary to account for results that cannot be described adequately by other approaches. A two-dimensional model which allows gas-phase contact to multiple rings from the compacts, possibly incorporating a trapping model, may also help to explain some of the complex profiles.

4.1.1   Analytical Diffusion Model

As described in (Humrickhouse et al. 2016), there is an analytical model that can describe radial diffusion through a hollow cylinder. This model is fast and has been implemented in a general fashion. There are, however, some drawbacks to this model. First, it cannot be used directly with a source-term containing region, and also requires a nonzero inner radius, so it is not directly applicable to the compact; though it can model sections of the compact. Second, and more importantly, the model is highly dependent on the time-dependent boundary conditions. Third, the model assumes a single diffusion coefficient across the ring, with no temperature-dependent diffusivity allowed, limiting its applicability where temperature gradients exist across the rings. Fourth, the model requires summations of infinite series of exponentials, which in practical application contain very few terms small enough to represent as an IEEE-754 double-precision number.

This model may be used to fit diffusivities where there is already known a reasonable approximation of the time-dependent concentration boundary conditions.

4.1.2   Finite-element Radial Diffusion Model

The BISON fuel-performance code now has sufficient built-in physics to model the radially symmetric case including sorption isotherms, including the time-dependent temperature profiles estimated by Hawkes (2016). Advances in model stability have been made throughout the last year to the point that a numerical model is robust enough to be incorporated into nonlinear curve-fitting, so long as the parameter set is reasonably constrained. While very low diffusivities can be computationally prohibitive at this point, many reasonable diffusivity ranges can be simulated on the order of a few minutes, leaving only minor complications in the way of diffusion coefficient estimation. The output from this model can be used as a boundary condition for the analytical fit as well, though given the drawbacks of the analytical fit, this may not be practically useful.

The results of this approach are shown in Figure 7, where the ^{134}Cs and ^{137}Cs measurements from Compacts 1-3 and 1-4 (Hunn et al. 2020) and the overall ^{134}Cs and ^{137}Cs IR inventory from the mass balance report (Stempien et al. 2018) were fit together to simultaneously obtain a temperature-dependent diffusivity and sorptivity. It is clear from the model fit that Fickian diffusion through the IR is not the primary source of activity in the OR and SR. The parameters obtained by the combined fit have been applied to models of the other capsules for comparison. Future work will be to fit transport models like this to each capsule individually and compare the results across capsules. Additional data may be available from compacts which underwent a separate heating test before having an R-DLBL analysis performed. The one-dimensional model needs to have an additional step taken without the rings to simulate transport and release from those compacts if these data are to be used.

Trapping physics can be added in a straightforward manner, though this may increase uncertainty in model fitting as there are now more parameters necessary to solve for.

4.1.3   Two-dimensional Finite Element Model

For several reasons, a two-dimensional finite-element model is desirable. First, the concentration increases on the outside of the rings have been speculated to originate from back-diffusion due to some process which would presumably transport material around, as opposed to through, the rings. This would most likely be due in part to axial transport in the gas phase around the rings. Second, the temperature profiles of the capsules are not uniform, and though the differences may not be large, it may help to explain the differences in observed concentrations between midplane and top and bottom end ring destructive analysis profiles. Due to the computational costs associated with the two-dimensional model, fitting to this model may not be practical, though it may be possible by leveraging High Performance Computing resources. This model will be useful in the modeling of silver.

Physics that should be implemented in a two-dimensional model are basic correlation-based natural convection/diffusion in the gas phase, and trapping/solubility in the solid phase. Together, these physics allow permeation modeling, which is the most likely candidate to explain the observed concentration profiles for silver, strontium, and europium. Exploring the physically relevant parameter space for these processes should provide insight as to whether some of the proposed mechanisms of transport have merit.

5.   CONCLUSIONS

Measured concentration profiles and overall ring concentrations are now available for the seven standard capsules and one of the five FB capsules in the AGR 3/4 experiment, and each capsule has been evaluated for its potential use in determining transport parameters for relevant fission products. Many of the compact and IR profiles appear to be suitable for use in estimating effective (temperature-dependent) Fickian diffusivities for cesium, with some profiles appearing to be suitable for strontium and europium. The OR profiles are generally less promising. SR average concentrations are available, though they are not likely to be useful in fitting. Preliminary estimates are available for cesium transport parameters in Capsule 1, and work is underway to fit to the data in a more rigorous, automated approach.

The general model framework described in (Riet and Stempien 2022) has been revised and incorporated into the BISON fuel-performance code. It is now capable of simulating time-dependent temperature profiles and is stable enough to use in standard optimization routines.

Advanced models appear to be necessary, especially to account for radially increasing concentration profiles in strontium and europium, and the elevated concentrations found on the outside of the rings in several capsules for all isotopes of interest. The recently implemented two-dimensional modeling is necessary to address the theory that vapor-phase transport is the cause of the high concentrations observed between the IR and OR and on the outside of the OR in Capsules 3, 4, 5, 7, 8, 10, and 12. Future work will incorporate the two-dimensional modeling efforts into the above-described BISON model and evaluate the speculated transport mechanisms.

6. REFERENCES

Collin, Blaise P. 2015a. "AGR-3/4 Irradiation Experiment Test Plan." Idaho National Laboratory Report, PLN-3867: INL/MIS-11-22351.

Collin, Blaise P., Paul A. Demkowicz, David A. Petti, Grant L. Hawkes, Joe Palmer, Binh T. Pham, Dawn M. Scates, and James W. Sterbentz. 2018. "The AGR-3/4 Fission Product Transport Irradiation Experiment." Nuclear Engineering and Design 327 (December 2017): 212–27. https://doi.org/10.1016/j.nucengdes.2017.12.016.

Collin, Blaise P. 2015b. "AGR-3/4 Irradiation Test Final As-Run Report." Idaho National Laboratory, INL/EXT-15-35550. https://inldigitallibrary.inl.gov/sites/sti/sti/6305200.pdf.

Demkowicz, Paul Andrew, John D. Hunn, Robert N. Morris, Isabella J. van Rooyen, Tyler J. Gerczak, Jason M. Harp, and Scott A. Ploger. 2015. "AGR-1 Post Irradiation Examination Final Report." Idaho National Laboratory Report, INL/EXT-15-36407. https://www.osti.gov/biblio/1236801%0Ahttps://www.osti.gov/servlets/purl/1236801.

De Maria, G., and V. Piacente. 1974. "Vapor Pressures of Calcium and Strontium by Transpiration Method." The Journal of Chemical Thermodynamics 6 (1): 1–7. https://doi.org/10.1016/0021-9614(74)90200-6.

Harp, Jason M, John D Stempien, and Paul A Demkowicz. 2020. "Gamma Spectrometry Examination of the AGR-3/4 Irradiation." Idaho National Laboratory Report, INL/EXT-20-58254.

Hawkes, Grant L. 2016. "AGR-3/4 Daily As-Run Thermal Analyses." Idaho National Laboratory, ECAR-2807.

Helmreich, Grant W, John D Hunn, Fred C Montgomery, and Darren J Skitt. 2021. "Radial Deconsolidation and Leach-Burn-Leach of AGR-3/4 Compacts 8-4 and 7-4," ORNL/TM-2021/2178.

Helmreich, Grant W, John D Hunn, Fred C Montgomery, and Darren J Skitt. 2022. "Radial Deconsolidation and Leach-Burn-Leach of AGR-3/4 Compacts 1-3, 4-3, 10-1, and 10-2," ORNL/TM-2022/2586.

Humrickhouse, Paul W., Blaise P. Collin, Grant L. Hawkes, Jason M. Harp, Paul A. Demkowicz, and David A. Petti. 2016. "Modeling and Analysis of Fission Product Transport in the AGR-3/4 Experiment." In HTR, 863–77. www.journal.uta45jakarta.ac.id.

Hunn, John D., and Andrew K. Kercher. 2006. "Results from ORNL Characterization of Nominal 350 Um LEUCO Kernels from the BWXT G73V-20-69303 Composite." Oak Ridge National Laboratory, ORNL/TM-2006/552.

Hunn, John D., Richard A. Lowden, James H. Miller, Brian C. Jolly, Michael P. Trammell, Andrew K. Kercher, Fred C. Montgomery, and Chinthaka M. Silva. 2014. "Fabrication and Characterization of Driver-Fuel Particles, Designed-to-Fail Fuel Particles, and Fuel Compacts for the US AGR-3/4 Irradiation Test." Nuclear Engineering and Design 271: 123–30. https://doi.org/10.1016/j.nucengdes.2013.11.020.

Hunn, John D., Fred C. Montgomery, Darren J. Skitt, and Grant W. Helmreich. 2020. "Radial Deconsolidation and Leach-Burn-Leach of AGR-3/4 Compacts 1-4 and 10-4." Oak Ridge National Laboratory, ORNL/TM-2020/1707.

Hunn, John D., Michael P. Trammell, and Fred C. Montgomery. 2011. "Data Compilation for AGR-3/4 Matrix Ring Blank Lot ARB-B1." Oak Ridge National Laboratory, ORNL/TM-2011/272.

Hunn, John D, and Richard A Lowden. 2007. "Data Compilation for AGR-3/4 Driver Fuel Coated Particle Composite LEU03-09T Revision 0." Oak Ridge National Laboratory 27: ORNL/TM-2007/019.

Hunn, John D, and James H Miller. 2009. "Data Compilation for AGR-3/4 Designed-to-Fail (DTF) Fuel Particle Batch LEU04-02DTF" 27: ORNL/TM-2008/193.

IAEA. 1997. "Fuel Performance and Fission Product Behaviour in Gas Cooled Reactors." International Atomic Energy Agency Report, IAEA-TECDOC-978.

INL. 2011. "ATR Advanced Gas Reactor (AGR-3/4) Capsule 3 Assembly and Details." Idaho National Laboratory, DWG-602703: Rev. 3.

INL. 2022. "Technical Program Plan for INL Advanced Reactor Technologies Advanced Gas Reactor Fuel Development and Qualification Program PLN-3636."

Kercher, Andrew K., Brian C. Jolly, Fred C. Montgomery, G. W. Chinthaka, M. Silva, and John D. Hunn. 2011. "Data Compilation for AGR-3/4 Particle Batch LEU03-07DTF." Oak Ridge National Laboratory, April: ORNL/TM-2011/109.

Lindsay, Alexander D, Derek R Gaston, Cody J Permann, Jason M Miller, David Andrš, Andrew E Slaughter, Fande Kong, et al. 2022. "MOOSE: Enabling Massively Parallel Multiphysics Simulation." SoftwareX 20: 101202. https://doi.org/https://doi.org/10.1016/j.softx.2022.101202.

Myers, B. F., and W. E. Bell. 1979. "Cesium Transport Data for HTGR Systems." General Atomics Report, GA-A13990.

Pittoni, Paola G., Yao Yuan Chang, and Shi Yow Lin. 2012. "The Effect of Interfacial Morphology on Wetting of Graphite by Molten Silver at High Temperature." Journal of Materials Science 47 (24): 8395–8403. https://doi.org/10.1007/s10853-012-6795-2.

Riet, Adriaan A. 2022. "Reconstruction of Fission Product Distribution from Tomographic Scans in TRISO Fuel Graphitic Matrix and Nuclear Grade Graphites." Idaho National Laboratory, INL/RPT-22-67635.

Riet, Adriaan A, and John D Stempien. 2022. "Comparison of AGR-3 / 4 Fission Product Transport Model to Measurements and Extraction of Diffusivities via Analytical Fits." Idaho National Laboratory, INL/RPT-22-69040.

Skerjanc, William F. 2016. "AGR-3/4 Irradiation Test Predictions Using PARFUME." Idaho National Laboratory Report, INL/EXT-16-38280.

Spedding, F H, J J Hanak, and A H Daane. 1958. "The Preparation and Properties of Europium." Trans. Met. Soc. AIME. https://www.osti.gov/biblio/4311992.

Stempien, John D. 2017. "Radial Deconsolidation and Leach-Burn-Leach of AGR-3/4 Compacts 3-3, 12-1 and 12-3." Idaho National Laboratory Report, INL/EXT-17-43182.

Stempien, John D. 2021. "Measurement of Fission Product Concentration Profiles in AGR-3/4 TRISO Fuel Graphitic Matrix and Nuclear Graphites," INL/EXT-21-62863.

Stempien, John D, Paul A Demkowicz, Jason M Harp, and Philip L Winston. 2018. "AGR-3/4 Experiment Preliminary Mass Balance." Idaho National Laboratory, INL/EXT-18-46049.

Stempien, John D, Francine J Rice, Phil L Winston, and Jason M Harp. 2016. "AGR-3/4 Irradiation Test Train Disassembly and Component Metrology First Look Report." Idaho National Laboratory, INL/EXT-16-38005.

Sterbentz, James W. 2015. "JMOCUP As-Run Daily Physics Depletion Calculation for the AGR-3/4 TRISO Particle Experiment in ATR Northeast Flux Trap." Idaho National Laboratory, ECAR 2753.

Walton, Kyle L., Nathan S. Jacobson, Benjamin A. Kowalski, John D. Brockman, and Sudarshan K. Loyalka. 2021. "Sorption Isosteres and Isotherms of Silver on NBG-17 Graphite." Journal of Nuclear Materials 557: 153264. https://doi.org/10.1016/j.jnucmat.2021.153264.

Williamson, Richard L, Jason D Hales, Stephen R Novascone, Giovanni Pastore, Kyle A Gamble, Benjamin W Spencer, Wen Jiang, et al. 2021. "BISON: A Flexible Code for Advanced Simulation of the Performance of Multiple Nuclear Fuel Forms." 207 (7): 954–80. https://doi.org/10.1080/00295450.2020.1836940.